Melting of heavy vector mesons and quasinormal modes in a finite density plasma from holography

Luis A. H. Mamani,[1,*] Defu Hou,[2,†] and Nelson R. F. Braga[3,‡]

[1]*Centro de Ciências Exatas Naturais e Tecnológicas, Universidade Estadual da Região Tocantina do Maranhão, Rua Godofredo Viana 1300, 65901- 480 Imperatriz, Maranhão, Brazil*

[2]*Institute of Particle Physics and Key Laboratory of Quark and Lepton Physics (MOS), Central China Normal University, Wuhan 430079, People's Republic of China*

[3]*Instituto de Física, Universidade Federal do Rio de Janeiro, Caixa Postal 68528, RJ 21941-972, Brazil*

(Received 30 April 2022; accepted 7 June 2022; published 21 June 2022)

In this work, we investigate, for the first time, the melting of charmonium states within a holographic QCD model in the context of Einstein-Maxwell-dilaton theory. In the dual field theory, the model describes the heavy mesons inside a finite temperature and density medium. First, we calculate the spectrum at zero temperature. Then, at finite temperature, we obtain the spectral functions, where the heavy vector meson are represented by peaks. We show that the charmonium melts down at temperatures above the confinement/deconfinement temperature of the quark-gluon plasma. We also observe that the chemical potential speeds up the melting process. In the gravitational side of the theory, we solve the perturbation equations in the hydrodynamic limit. From this result, we read off the diffusion coefficient, then the quark number susceptibility. We show that the quark number susceptibility computed in this way does not blow up at the critical end point. We interpret this result as the lack of backreaction on the background by the action describing the vector mesons. To get the quasinormal frequencies, we solve the perturbation equations numerically. We report the emergence of a new mode whose real part increases rapidly at a certain value of the chemical potential, while its imaginary part decreases with the increasing of the chemical potential. Finally, by comparing against results obtained in the conformal plasma, we observe that the real part of the frequency increases, while the imaginary part decreases when we consider the nonconformal plasma.

DOI: 10.1103/PhysRevD.105.126020

I. INTRODUCTION

Heavy-ion collisions allow us to investigate QCD in the laboratory. The medium created after $(A + A)$ collisions, known as the quark gluon plasma (QGP), is very hot and dense with extremely short lifetime (∼5–10 fm/c). In this plasma, light quarks and gluons interact strongly but are not confined inside hadrons. It is believed that one can use heavy mesons as probes in order to extract relevant information of the medium in such extreme conditions [1–3]. The idea is that, in contrast to hadrons made of the light quarks [u (up), d (down), and s (strange)] that dissociate at the critical temperature [4] when the plasma is formed, heavy mesons, made of c (charm) or b (bottom) quarks survive at higher temperatures. The fraction of heavy mesons produced in a heavy ion collision may serve as an important source of information about the preexisting QCD. That is the motivation for understanding how the properties of the QGP, like temperature and density, affect the dissociation of charmonium.

An important framework to investigate the dissociation of heavy vector mesons is the use of holographic models inspired in the anti-de Sitter (AdS)/CFT correspondence. In its original form, the AdS/CFT correspondence states a duality between super-Yang-Mills theory living on a flat four-dimensional spacetime, with a supergravity theory living on an $AdS_5 \times S^5$ spacetime [5] (see also Refs. [6,7]). A phenomenological approach to gauge/gravity duality, now called AdS/QCD, was proposed in Refs. [8–10]. Since then, a considerable number of papers were published with similar phenomenological models; see, for

*luis.mamani@uemasul.edu.br
†houdf@mail.ccnu.edu.cn
‡braga@if.ufrj.br

instance, Refs. [11–20] and references therein. It is worth stressing that, in this so-called bottom-up AdS/QCD approach, the geometry is kept as AdS space-time, neglecting backreactions of the fields introduced in the models on the geometry. The investigation of hadron dissociation in a thermal medium in the framework of holography was carried out, for instance, in Refs. [21–29]; see also references therein. Finite temperature effects in the dual field theory are related to black hole thermodynamics in the gravitational field theory, while finite density effects are related to the charge of the black hole solution. Following the holographic dictionary, one may extract relevant information about the dissociation process in the dual field theory. Heavy vector mesons have been studied following a bottom-up holographic approach in Refs. [30–36].

On the other hand, a different approach is followed in the construction of the so-called top-down holographic models. In this case, the gravitational backgrounds are obtained solving Einstein's equations. In other words, backreaction of the dilaton field on the metric is not neglected. Examples of such Einstein-dilaton models can be found, for instance, in Refs. [37–45] and references therein. Investigations of finite density and magnetic field effects in the context of the Einstein-Maxwell-dilaton models appear, for example, in Refs. [46–53].

In this work, we follow the Einstein-Maxwell-dilaton holographic approach in order to analyze the dissociation of heavy charmonium in a plasma with finite temperature and density. We analyze the thermal spectrum and the quasinormal modes and compare our findings with results available in the literature. The paper is organized as follows. In Sec. II, we present a brief review of the holographic model we are going to work with. Section III is devoted to investigating the charmonium states within the holographic model. We calculate the spectrum at zero temperature; then, we introduce finite temperature effects through a black hole embedded in the dual gravitational background. We get the equations of motion describing two sectors: longitudinal and transverse, which we write in the Schrödinger-like form. In turn, in Sec. IV, we investigate finite temperature and density effects on the effective potential arising in the Schrödinger-like equation. The analysis of the spectral functions for selected values of the temperature and chemical potential are presented and discussed in Sec. V. It is also interesting to solve the equations of motion using perturbative techniques. This is possible in the so-called hydrodynamic limit where the energy and wave number are smaller than the temperature. We present this analysis in Sec. VI. From the solutions in the hydrodynamic limit, we calculate the correlation functions in the dual field theory. These results allow us to calculate the quark-number susceptibility that we present in Sec. VII. Moreover, it is worth solving the equations of motion numerically to get the quasinormal frequencies in the gravitational side of the duality. We implement this procedure in Sec. VIII. Finally, our conclusions are presented in Sec. IX. We present complementary material in Appendix.

II. HOLOGRAPHIC MODEL

In the following, we define the holographic QCD model we are going to work with proposed in Ref. [46]. The five-dimensional action describing the finite density medium in the dual field theory is given by

$$S_b = \frac{1}{16\pi G_5}\int d^5x\sqrt{-g}\Big(R - \frac{f(\phi)}{4}F^2 - \frac{1}{2}(\partial^m\phi)(\partial_m\phi) - V(\phi)\Big), \tag{1}$$

where G_5 is the gravitational constant in five dimensions, ϕ is the scalar field and $V(\phi)$ its potential, $f(\phi)$ represents the kinetic function (nonminimal coupling), and $F^2 = F_{mn}F^{mn}$, with $F_{mn} = \partial_m A_n - \partial_n A_m$, where A_m is the gauge field. The corresponding equations of motion are given by

$$G_{mn} - \frac{1}{2}(\partial_m\phi)(\partial_n\phi) + \frac{g_{mn}}{4}(\partial^p\phi)(\partial_p\phi) + \frac{g_{mn}}{2}V + \frac{f}{2}\left(\frac{g_{mn}}{4}F^2 - F_{mp}F^p_n\right) = 0, \tag{2a}$$

$$\partial_m(\sqrt{-g}fF^{nm}) = 0, \tag{2b}$$

$$\frac{1}{\sqrt{-g}}\partial_m(\sqrt{-g}\partial^m\phi) - \partial_\phi V - \frac{f}{4}F^2 = 0, \tag{2c}$$

where G_{mn} is the Einstein tensor. Equations (2a)–(2c) are the Einstein equations, the Maxwell equations, and the Klein-Gordon equation, respectively. As can be seen, these equations are coupled and must be solved simultaneously.

As we are interested in the finite temperature and density plasma, we need to consider the black hole solution of these set of equations. We consider the ansatz

$$ds^2 = \frac{1}{\zeta(z)^2}\left(-g(z)dt^2 + \frac{1}{g(z)}dz^2 + dx_i dx^i\right),$$
$$A_t = A_t(z), \qquad A_{x^1} = A_{x^2} = A_{x^3} = A_z = 0,$$
$$\phi = \phi(z), \tag{3}$$

where $g(z)$ is the horizon (blackening) function, $\zeta(z)$ is a function related to the warp factor, and $A_t(z)$ is the nonzero component of the gauge field, which gives rise to finite density in the dual field theory. The black hole solutions are characterized by the presence of an event horizon, z_h, where the horizon function vanishes, $g(z_h) = 0$. Thus, the holographic coordinate belongs to the interval $0 \le z \le z_h$. Considering the ansatz (3), the Einstein equations (2a) reduce to

$$\frac{\zeta''}{\zeta}-\frac{1}{6}\phi'^2=0,$$
$$g''-\frac{3\zeta'}{\zeta}g'-f(A_t'\zeta)^2=0,$$
$$V-\frac{f}{2}(\zeta^2A_t')^2+3\zeta^5\left(\frac{g\zeta'}{\zeta^4}\right)'=0. \tag{4}$$

Meanwhile, the nontrivial Maxwell equation is given by

$$\left(\frac{f}{\zeta}A_t'\right)'=0. \tag{5}$$

As is usual in this kind of holographic models, the Klein-Gordon equation becomes redundant and can be obtained from the Einstein equations. We point out that these equations are the same as presented in Ref. [46] written in a compact form.

In turn, regularity conditions imposed on the horizon function and gauge field at the horizon require that

$$g(z_h)=0, \quad \text{and} \quad A_t(z_h)=0. \tag{6}$$

Meanwhile, at the boundary, the horizon function must reduce to the unity, $g(0)=1$, while the asymptotic expansion of the gauge field takes the form

$$A_t=\mu-\rho z^2+\mathcal{O}(z^4), \qquad z\to 0, \tag{7}$$

where μ is the chemical potential and ρ is the baryon density. Thus, once we solve Eq. (5), we expand the solution close to the boundary to read off the chemical potential and baryon density by comparing the solution against the asymptotic expansion (7).

The coupled Eqs. (4) may be solved following different approaches; see the discussion in Refs. [41–43] and references therein. Thus, the warp factor and the kinetic function are given by [46,54]

$$\zeta=\frac{z}{\ell}e^{-\mathcal{A}(z)}, \qquad f=e^{-cz^2-\mathcal{A}(z)}, \tag{8}$$

where $\mathcal{A}(z)$ is a function defined by

$$\mathcal{A}(z)=-\frac{c}{3}z^2-bz^4. \tag{9}$$

It is interesting to calculate the asymptotic expansion of the functions ζ and f close to the boundary, which are given by

$$\zeta=\frac{z}{\ell}\left(1+\frac{c}{3}z^2+\left(b+\frac{c^2}{18}\right)z^4\cdots\right), \qquad z\to 0$$
$$f=1-\frac{2}{3}cz^2+\left(b+\frac{2c^2}{9}\right)z^4\cdots. \qquad z\to 0. \tag{10}$$

In Fig. 1, we display a plot for functions $\mathcal{A}$ (right panel) and f (left panel) setting $c=1$ and considering two values for the parameter b, positive ($b=1$) and negative ($b=-1$). This plot was motivated by the discussion of Ref. [47] in which a negative signal for b was considered. As can be seen, the kinetic function increases with z for $b>0$ (blue line), while it decreases with z for $b<0$ (red line). In turn, the function $\mathcal{A}$ decreases with z for $b>0$ (blue line), while it increases with z for $b<0$ (red line).

Let us turn our attention to the free parameters c and b. They were fixed by phenomenology in Ref. [46], their corresponding values are

$$c=1.16\ \text{GeV}^2, \qquad b=0.273\ \text{GeV}^4. \tag{11}$$

We can now solve the background equations by plugging (8) into (5). Thus, we get a solution for the gauge field

$$A_t=c_2+\frac{c_1}{2c\ell}e^{cz^2}. \tag{12}$$

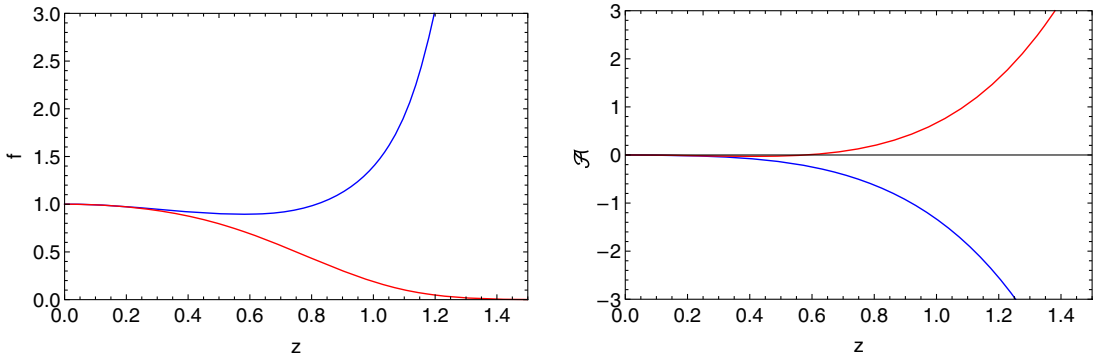

FIG. 1. Left: the kinetic function as a function of z for $b=1$ (blue) and $b=-1$ (red) setting $c=1$. Right: the function $\mathcal{A}$ as a function of z for $b=1$ (blue) and $b=-1$ (red) setting $c=1$.

We fix the constants using the boundary conditions. Hence, the gauge field and its expansion close to the boundary are given by

$$A_t = \frac{e^{cz^2} - e^{cz_h^2}}{1 - e^{cz_h^2}}\mu, \quad A_t = \mu - \frac{c\mu}{e^{cz_h^2} - 1}z^2 + \mathcal{O}(z^4). \tag{13}$$

From the last expression, we read off the baryon (charge) density ρ by comparing against (7). It is worth pointing out that the gauge field does not depend on the parameter b. Analogously, we can get a solution for the horizon function, $g(z)$. Hence, the thermodynamic variables like the temperature and entropy density are defined by

$$T = -\frac{g'(z_h)}{4\pi}, \qquad s = \frac{1}{4G_5\zeta^3(z_h)}. \tag{14}$$

A plot of the temperature as a function of z_h is displayed in the left panel of Fig. 2. As can be seen, the behavior of the temperature depends on the value of the chemical potential. For $\mu = 0$, there is a global minimum; this point splits up the large black hole phase (stable phase) and the small black hole phase (unstable phase). Moreover, for $\mu > 0$, there are a local minimum and a local maximum, which merge in the same point for a critical value of the chemical potential, μ_{CEP}, with the corresponding critical temperature, T_{CEP}. The point $(\mu_{\mathrm{CEP}}, T_{\mathrm{CEP}})$ defines the critical end point in the $\mu - T$ plane.

To calculate the phase diagram, we need the free energy density, which is calculated using the first law of thermodynamics,

$$\frac{d\mathcal{F}}{dT} = -s. \tag{15}$$

Then, the integral representation for the free energy density is given by

$$\mathcal{F} = \int_{z_h}^{\infty} s(\tilde{z})\left(\frac{dT(\tilde{z})}{d\tilde{z}}\right)d\tilde{z}. \tag{16}$$

The last result considers the free energy of the thermal gas, which is considered to be zero. The numerical results of the phase diagram are displayed in the right panel of Fig. 2. In this way, we finish the short review of the holographic model we are going to work with; for additional discussions and details, see Ref. [46]. In the following, we are going to calculate the spectrum of heavy-vector mesons on this background; then, we investigate their melting.

III. HEAVY VECTOR MESONS

The heavy-vector mesons in the dual field theory are described by five-dimensional gauge field whose action is given by

$$S_m = -\frac{1}{16\pi G_5}\int d^5x\sqrt{-g}\frac{f(\phi)}{4}F_V^2, \tag{17}$$

where the gauge field is defined by $F_{Vmn} = \partial_m A_n - \partial_n A_m$ and $f(\phi)$ is the kinetic (nonminimal) function defined in Eq. (8). It is worth mentioning that in the probe limit the contribution of the matter field to the energy-momentum tensor is neglected. In the dual field theory, this corresponds to the quenched approximation, in which the quark loops in the Feynman diagrams are neglected [57]. The equations of motion obtained from this action are given by

$$\partial_m(\sqrt{-g}fF_V^{mn}) = 0. \tag{18}$$

Let us focus in the zero temperature case where the background metric (3) reduces to

$$ds^2 = \frac{1}{\zeta(z)^2}(dz^2 + dx_\mu dx^\mu). \tag{19}$$

To simplify the analysis, we are going to work in the radial gauge $A_z = 0$. Setting $n = z$ in (18), we get the constraint $\partial_\alpha A^\alpha = 0$. In turn, setting $n = \nu$, we get the equation describing the heavy-vector mesons, which may be written as

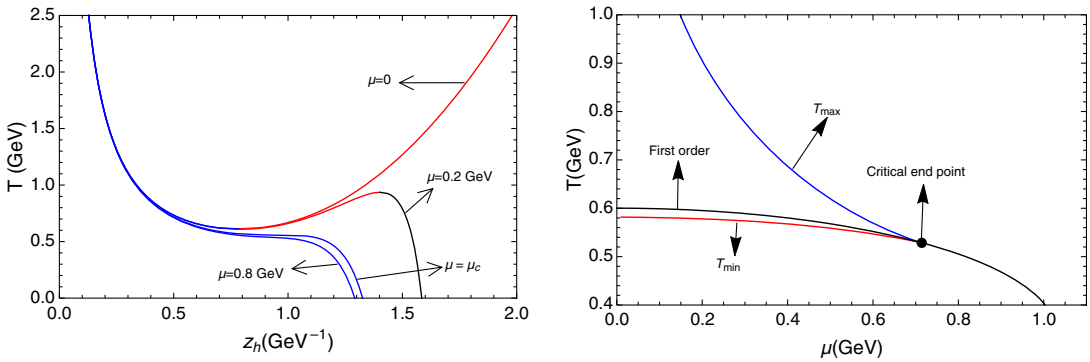

FIG. 2. Left: the temperature as a function of z_h for different values of the chemical potential. Right: the phase diagram of the holographic model, where the critical end point is highlighted.

$$\frac{\zeta}{f}\partial_z\left(\frac{f}{\zeta}\partial_z A^\nu\right)+\Box A^\nu=0. \tag{20}$$

Introducing the Fourier transform on the gauge field

$$A_\nu(z,x^\mu)=\int\frac{d^4k}{(2\pi)^4}e^{ik_\alpha x^\alpha}A_\nu(z,k), \tag{21}$$

it transforms as $A^\nu(x^\mu,z)\to A^\nu(k^\mu,z)$. The equation may be rewritten in the Schrödinger-like form using the transformation $A_\nu=\xi_\nu e^{-B}\psi$, where ξ_ν is a polarization vector and $2B=\ln(f/\zeta)$; thus, the equation becomes

$$-\partial_z^2\psi+V\psi=m_n^2\psi, \tag{22}$$

where we have replaced $\Box\to m_n^2$ and V is the potential given by

$$V=(\partial_z B)^2+\partial_z^2 B. \tag{23}$$

As the background was already fixed, we may solve the eigenvalue problem using a shooting method, for example. It is worth pointing out that the ratio f/ζ does not depend on the parameter b; for that reason, the spectrum is insensitive to this parameter. The way this holographic model was built allows us to get an analytic solution for the mass spectrum, which is given by

$$m_n^2=4c(n+1),\quad n=0,1,2,\cdots \tag{24}$$

In the sequence, we fix the free parameter by fitting this formula with the first two resonances of charmonium available from experimental data [58], and by doing so, we get $c=1.46\ \mathrm{GeV}^2$ [59]. A plot of the potential is displayed in Fig. 3. The numerical results for the spectrum compared against charmonium experimental data are displayed in Table I.

Having fixed the parameter c, the critical end point in the phase diagram lies in a different position in relation to the one obtained in Ref. [46]. Considering $c=1.46$ GeV, it lies at $(\mu_{\mathrm{CEP}},T_{\mathrm{CEP}})=(0.708\ \mathrm{GeV},0.559\ \mathrm{GeV})$. Finally,

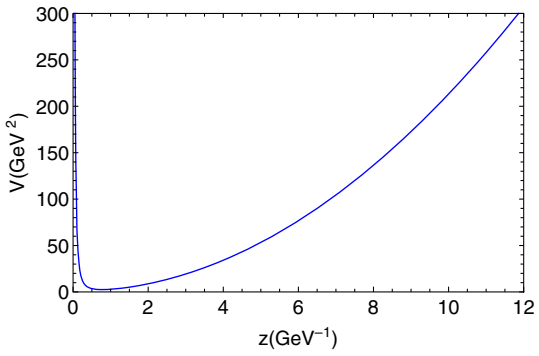

FIG. 3. The potential of the Schrödinger-like equation.

TABLE I. The mass of the vector mesons (in MeV) obtained in the holographic model compared against the experimental results from the Particle Data Group [58].

n	Holographic model	Charmonium experimental [58]
0	2420	3096.916 ± 0.011
1	3422	3686.109 ± 0.012
2	4191	4039 ± 1
3	4839	4421 ± 4

the eigenvalue problem solved at zero temperature has real solutions. However, we shall see below that the black hole embedded in the geometry will change the eigenvalues into complex. These states shall be interpreted as quasiparticles characterized by the complex frequencies whose real part is interpreted as the thermal mass, while their imaginary part is related to the decay rate of these states. The corresponding field solutions are called the quasinormal modes. They are the finite temperature version of the normal modes that describe the states at zero temperature.

On the other hand, in the black hole background, the problem changes completely due to Poincaré symmetry breaking. To simplify the analysis, we are going to work in the radial gauge, $A_z=0$, and consider plane wave solutions in the form $A_\mu(x^\nu,z)=e^{-i\omega t+iqx^3}A_\mu(\omega,q,z)$, where we are considering the direction of propagation $q^\mu=(\omega,0,0,q)$. Thus, the equations of motion (18) can be written in the form

$$\partial_z\left(\frac{f}{\zeta}\partial_z A_t\right)-\frac{qf}{g\zeta}(qA_t+\omega A_{x^3})=0, \tag{25a}$$

$$\omega\partial_z A_t+qg\partial_z A_{x^3}=0, \tag{25b}$$

$$\partial_z\left(\frac{gf}{\zeta}\partial_z A_{x^3}\right)+\frac{\omega f}{g\zeta}(qA_t+\omega A_{x^3})=0, \tag{25c}$$

$$\frac{g\zeta}{f}\partial_z\left(\frac{fg}{\zeta}\partial_z A_\alpha\right)+(\omega^2-q^2g)A_\alpha=0.\quad(\alpha=x^1,x^2). \tag{25d}$$

Next, we write the last equations in terms of gauge-invariant fields defined by $E_{x^1}=\omega A_{x^1}$, $E_{x^2}=\omega A_{x^2}$, and $E_{x^3}=qA_t+\omega A_{x^3}$, as

$$\frac{g\zeta}{f}\partial_z\left(\frac{fg}{\zeta}\partial_z E_\alpha\right)+(\omega^2-q^2g)E_\alpha=0,\ \ (\alpha=x^1,x^2), \tag{26a}$$

$$\frac{g\zeta}{f}\partial_z\left(\frac{fg}{\zeta(\omega^2-q^2g)}\partial_z E_{x^3}\right)+E_{x^3}=0. \tag{26b}$$

Equations (26a) represent the propagation in the transverse direction, while Eq. (26b) represents the propagation along the longitudinal direction. It is also possible to rewrite each of these equations into a Schrödinger-like form. The

Schrödinger-like form allows us to investigate the potential and how it will be deformed by the temperature and chemical potential, which is interpreted as the melting of the quasiparticle states. To get the Schrödinger-like equation we need to define the tortoise coordinate, $\partial_{r_*} = -g(z)\partial_z$, and the transformation $E_\alpha = e^{-B_T}\psi_\alpha$. Thus, Eq. (26a) becomes

$$-\partial_{r_*}^2\psi_\alpha + V_T\psi_\alpha = \omega^2\psi_\alpha, \tag{27}$$

where V_T is the transverse potential defined by

$$V_T = q^2 g + (\partial_{r_*}B_T)^2 + \partial_{r_*}^2 B_T, \tag{28}$$

with $2B_T = \ln(f/\zeta)$. By restoring the holographic coordinate, the transverse potential becomes

$$V_T = g(q^2 + g(\partial_z B_T)^2 + \partial_z(g\partial_z B_T)). \tag{29}$$

As can be seen, the transverse potential is zero at the horizon, where $g(z_h) = 0$. In the same way, we may write Eq. (26) in the Schrödinger-like form by using the tortoise coordinate and the transformation $E_{x^3} = e^{-B_L}\psi_{x^3}$ getting

$$-\partial_{r_*}^2\psi_{x^3} + V_L\psi_{x^3} = \omega^2\psi_{x^3}, \tag{30}$$

where V_L is the longitudinal potential defined by

$$V_L = q^2 g + (\partial_{r_*}B_L)^2 + \partial_{r_*}^2 B_L, \tag{31}$$

with $2B_L = \ln(f/[\zeta(\omega^2 - q^2 g)])$. Restoring the holographic coordinate, the longitudinal potential becomes

$$V_L = g(q^2 + g(\partial_z B_L)^2 + \partial_z(g\partial_z B_L)). \tag{32}$$

Note that V_T and V_L are the same when $q = 0$. Note also that the longitudinal potential vanishes at the horizon. The Schrödinger-like form of the differential equations (27) and (30) may be solved close to the horizon where $g(z_h) = 0$. Thus, we have the solutions for both sectors,

$$\psi_j \sim \mathcal{C}_j e^{-i\omega r_*} + \mathcal{D}_j e^{+i\omega r_*}, \quad (j = \alpha, x^3) \tag{33}$$

where the first solution is interpreted as an incoming wave falling into the black hole while the second one is interpreted as an outgoing wave coming from the black hole interior. To be more precise, we may calculate the incoming $\psi_j^{(-)}$ and outgoing $\psi_j^{(+)}$ solutions including a few subleading terms in the form

$$\psi_j^{(+)} = e^{+i\omega r_*}(a_{0j}^{(+)} + a_{1j}^{(+)}(z_h - z) + a_{2j}^{(+)}(z_h - z)^2 + \cdots) \tag{34a}$$

$$\psi_j^{(-)} = e^{-i\omega r_*}(a_{0j}^{(-)} + a_{1j}^{(-)}(z_h - z) + a_{2j}^{(-)}(z_h - z)^2 + \cdots). \tag{34b}$$

The coefficients $a_{0j}^{(\pm)}, a_{1j}^{\pm}, \cdots$, are given by $a_{0j}^{(\pm)} = 1$,

$$a_{1j}^{(\pm)} = \frac{a_{0j}^{(\pm)}}{2z_h(f'(z_h) \mp 2i\omega)}\left(2q^2 z_h - (1 + 2cz_h^2)f'(zh) + \delta_{jx^3}\frac{q^2 z_h (f'(z_h))^2}{\omega^2}\right),$$

$$\begin{aligned} a_{2\alpha}^{(\pm)} = {} & \frac{a_{0\alpha}^{(\pm)}}{8z_h^2(2\omega \pm if'(z_h))(5\omega \pm 4if'(z_h))}(6\omega^2 - 8q^4 z_h^2 + 8c^2 z_h^4\omega^2 + [8q^2(z_h + 2cz_h^3) \pm i(23 - 16cz_h^2 + 20c^2 z_h^4)\omega]f'(z_h) \\ & - 4(3 + 4c^2 z_h^4)f'(z_h)^2 + 8z_h[q^2 z_h \mp i(\omega + 2cz_h^2\omega)]f''(z_h)), \end{aligned}$$

$$\begin{aligned} a_{2x^3}^{(\pm)} = {} & \frac{a_{0x^3}^{(\pm)}}{8z_h^2\omega^4(2\omega \pm if'(z_h))(5\omega \pm 4if'(z_h))}((6 + 8c^2 z_h^4)\omega^6 - 8q^4 z_h^2\omega^4 + q^2 z_h\omega(\pm 25iq^2 z_h + 8(1 + 2cz_h^2)\omega)f'(z_h)^3 \\ & - 12q^4 z_h^2 f'(z_h)^4 + 4z_h\omega^4(3q^2 z_h \mp 2i\omega(1 + 2cz_h^2))f''(z_h) + [-8q^2 z_h^2\omega^2 f''(z_h) + 2\omega^2(q^4 z_h^2 \mp 5iq^2 z_h(1 + 2cz_h^2)\omega \\ & - 2(3 + 4c^2 z_h^4)\omega^2)]f'(z_h)^2 + [\omega(4q^2 z_h(1 + 2cz_h^2) \pm i(23 - 16cz_h^2 + 20c^2 z_h^4)\omega) \pm 26iq^2 z_h^2 f''(z_h)]\omega^3 f'(z_h)). \end{aligned} \tag{35}$$

On the other hand, we may solve the Schrödinger-like equations close to the boundary, where the normalizable $\psi_k^{(1)}$ and non-normalizable $\psi_k^{(2)}$ solutions are given by

$$\psi_j^{(1)} = z^{3/2}(b_{0j} + b_{2j}z^2 + b_{4j}z^4 + \cdots), \tag{36a}$$

$$\psi_j^{(2)} = z^{-1/2}(c_{0j} + c_{2j}z^2 + c_{4j}z^4\cdots) + d_j\psi_j^{(1)}\ln(z), \tag{36b}$$

where the coefficients are given by

$$b_{2j} = \frac{(q^2 - \omega^2)}{8}b_{0j}, \quad c_{4\alpha} = \frac{1}{64}(8c^2 - 3b_{0\alpha}(q^2 - \omega^2)^2)c_{0\alpha},$$
$$d_j = \frac{(q^2 - \omega^2)}{2}c_{0j}; \tag{37}$$

the coefficients b_{4j} and c_{4x^3} are complicated expressions, and for that reason, we do not write them here. Meanwhile,

we have the freedom to set $c_{2j} = 0$. The next step forward is to write the incoming and outgoing solutions as a linear combination of the normalizable and non-normalizable solutions:

$$\psi_j^{(+)} = \mathcal{A}_j^{(+)}\psi_j^{(2)} + \mathcal{B}_j^{(+)}\psi_j^{(1)}, \tag{38a}$$

$$\psi_j^{(-)} = \mathcal{A}_j^{(-)}\psi_j^{(2)} + \mathcal{B}_j^{(-)}\psi_j^{(1)}. \tag{38b}$$

Analogously, the normalizable and non-normalizable solutions may be written as a linear combination of the incoming and outgoing solutions in the form

$$\psi_j^{(2)} = \mathcal{C}_j^{(2)}\psi_j^{(-)} + \mathcal{D}_j^{(2)}\psi_j^{(+)}, \tag{39a}$$

$$\psi_j^{(1)} = \mathcal{C}_j^{(1)}\psi_j^{(-)} + \mathcal{D}_j^{(1)}\psi_j^{(+)}. \tag{39b}$$

The coefficients of the last equations are related through

$$\begin{pmatrix} \mathcal{A}_j^{(+)} & \mathcal{B}_j^{(+)} \\ \mathcal{A}_j^{(-)} & \mathcal{B}_j^{(-)} \end{pmatrix} = \begin{pmatrix} \mathcal{C}_j^{(2)} & \mathcal{D}_j^{(2)} \\ \mathcal{C}_j^{(1)} & \mathcal{D}_j^{(1)} \end{pmatrix}^{-1}. \tag{40}$$

These relations shall be useful below when we calculate the spectral functions; see Refs [22,23,25] for additional details.

IV. EFFECTIVE POTENTIAL

Let us start by investigating the case when $\mu = 0$. In this case, the plot of the temperature as a function of z_h, see the left panel of Fig. 2, has two branches: large and small black holes. Considering the stable regime, i.e., the large black hole branch, the temperature belongs to the interval $T_{\min} \leq T < \infty$. A plot of the potential as a function of the tortoise coordinate for selected values of the temperature setting $q = 0$ is displayed in the left panel of Fig. 4. As can be seen, for $T = T_{\min} = 0.612$ GeV (blue line), the potential has a small potential well; this means that probably we will not find quasiparticle states for this temperature. In turn, for $T = 0.7$ GeV (red dashed line) and $T = 0.8$ GeV (black dashed line), there is no potential well, meaning that the probability of finding quasiparticle states should be practically zero. It is worth comparing the potential at finite temperature against the potential at zero temperature displayed in Fig. 3. As can be seen, the temperature deforms the potential well. This deformation is interpreted as the dissociation of bound states, which are thermally at zero temperature.

Meanwhile, turning on the chemical potential, $\mu \neq 0$, there are three branches arising in the plot of the temperature as a function of z_h, as seen in the left panel of Fig. 2, depending on the value of μ. We displayed our numerical results for $\mu = 0.2$ GeV and the isotherm at $T = 0.8$ GeV in the right panel of Fig. 4. The first branch of Fig. 2, where the background is stable, is represented with a blue line. Meanwhile, the second branch, where the background is unstable, is represented with a red dashed line. The third branch, where we got a stable solution, is represented with a black dashed line. As can be seen in the right panel of Fig. 5, it is possible to find quasiparticle states in the third branch (black dashed line) because the potential displays a potential well, while in the second branch (red dashed line) they shall be in an unstable phase, while in the first branch (solid blue line), there are no quasiparticle states. In turn, it is also illustrative to show the effects of the chemical potential on the deformation of the potential well. In Fig. 5, we displayed the potential fixing the temperature at the isotherm $T = T_{\min} = 0.612$ GeV and varying the chemical potential for $q = 0$. As can be seen, the potential is also sensitive to the variation of the chemical potential.

In conclusion, increasing the temperature and the chemical potential, the melting process speeds up. It is also interesting to point out that these results are qualitatively equivalent to results obtained within the bottom-up

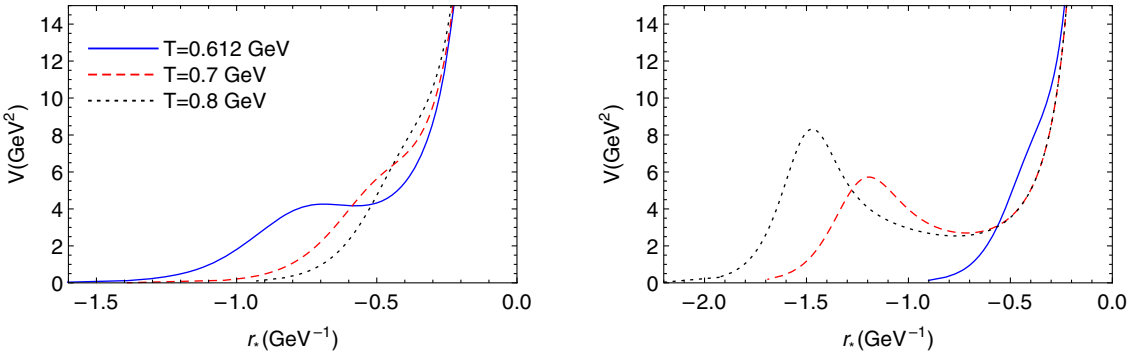

FIG. 4. Left: the potential as a function of the tortoise coordinate r_* for $\mu = 0$ and $q = 0$. The blue line represents the results for $T = T_{\min} = 0.612$ GeV, the red dashed line represents results for $T = 0.7$ GeV, and black dashed line represents results for $T = 0.8$ GeV. Right: the figure shows the potential as a function of r_* for $\mu = 0.2$ GeV and the isotherm $T = 0.8$ GeV setting $q = 0$. The blue line represents the large black hole branch, the red dashed line represents the second branch, and the black dashed line represents the third one. These branches can be seen in the left panel of Fig. 2.

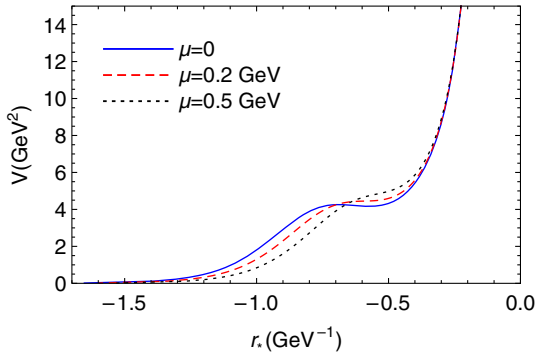

FIG. 5. The potential as a function of the tortoise coordinate r_* for $T = T_{\min} = 0.612$ GeV and different values of the chemical potential: $\mu = 0$ (blue line), $\mu = 0.2$ GeV (red dashed line), and $\mu = 0.5$ GeV (black dashed line).

holographic QCD models in the literature [22,23,25,32–36,60]; see also references therein. The difference of our results in relation to those is that the background we are working with was obtained solving the Einstein-Maxwell-dilaton equations.

V. SPECTRAL FUNCTIONS

To calculate the correlation functions, we need to determine the on-shell action; then, we use the Son-Starinets prescription [61] to read off the correlation functions. Let us start by writing the action (17) in the form

$$S_m = \frac{1}{16\pi G_5}\int d^5x\sqrt{-g}\frac{f(\phi)}{2}\partial_m A_n F_V^{mn}. \tag{41}$$

Plugging the components of the gauge field, the background metric (3), and the Fourier transform (21), the action may be rewritten in the form

$$S_m = \frac{1}{32\pi G_5}\int \frac{dqd\omega}{(2\pi)^2}\frac{f}{\zeta}(g\mathbf{A}(z,-k)\cdot\partial_z\mathbf{A}(z,k) - A_t(z,-k)\partial_z A_t(z,k))|_{z_0}^{z_h}, \tag{42}$$

where $\mathbf{A} = (A_{x^1}, A_{x^2}, A_{x^3})$ is a spatial vector. In terms of the gauge-invariant fields, this action becomes

$$S_m = -\frac{1}{32\pi G_5}\int \frac{dqd\omega}{(2\pi)^2}\frac{gf}{\zeta\omega^2}\left[\frac{\omega^2}{\omega^2-q^2g}E_{x^3}(z,-k)E'_{x^3}(z,k) + E_{x^1}(z,-k)E'_{x^1}(z,k) + E_{x^2}(z,-k)E'_{x^2}(z,k)\right]\Bigg|_{z_0}^{z_h}. \tag{43}$$

To get the correlation functions, it is useful to split up the gauge field as the product of two functions, one of them depending only on the holographic coordinate, $\mathcal{E}_j(z)$, and the other depending on the wave number $E_j^{(-)}(k)$,

$$E_j(z,k) = \mathcal{E}_j(z)E_j^{(-)}(k), \qquad (j = x^1, x^2, x^3), \tag{44}$$

where the function $\mathcal{E}_j$ is normalized such that $\lim_{z_0\to 0}\mathcal{E}_j(z_0) = 1$; we also consider the ingoing solution at the horizon such that we are computing the retarded Green's function. Thus, the on-shell action can be rewritten in the form

$$S_m = \frac{1}{32\pi G_5}\int \frac{dqd\omega}{(2\pi)^2}\frac{fg}{\zeta}\left[\frac{\omega^2}{\omega^2-q^2g}\left(\frac{q^2}{\omega^2}A_t^0(-k)A_t^0(k) + \frac{q}{\omega}A_t^0(-k)A_{x^3}^0(k) + \frac{q}{\omega}A_{x^3}^0(-k)A_t^0(k) + A_{x^3}^0(-k)A_{x^3}^0(k)\right)\mathcal{E}_{x^3}(z)\mathcal{E}'_{x^3}(z) + \sum_{\alpha=x^1,x^2}A_\alpha^0(-k)A_\alpha^0(k)\mathcal{E}_\alpha(z)\mathcal{E}'_\alpha(z)\right]\Bigg|_{z_0}^{z_h}. \tag{45}$$

The last expression can be written in a compact form,

$$S_m = \int \frac{dqd\omega}{(2\pi)^2}A_\mu^0(-k)\mathcal{F}^{\mu\nu}(z,k)A_\nu^0(k)|_{z_0}^{z_h}. \tag{46}$$

Thus, we get the current-current correlators using the Son-Starinets prescription $C_{\mu\nu}^R(k) = -2\eta_{\mu\gamma}\eta_{\nu\beta}\lim_{z_0\to 0}\mathcal{F}^{\gamma\beta}(z_0,k)$,

$$\frac{C_{tt}^R}{q^2} = \frac{C_{x^3x^3}^R}{\omega^2} = -\frac{C_{tz}^R}{q\omega} = -\frac{C_{zt}^R}{q\omega} = -\frac{N_c^2}{16\pi^2(\omega^2-q^2)}\lim_{z_0\to 0}\frac{1}{\zeta(z_0)}\mathcal{E}'_{x^3}(z)|_{z=z_0}, \tag{47a}$$

$$C_{\alpha\alpha}^R = -\frac{N_c^2}{16\pi^2}\lim_{z_0\to 0}\frac{1}{\zeta(z_0)}\mathcal{E}'_\alpha(z)|_{z=z_0}. \tag{47b}$$

To get these results, we have considered the fact that $g(z_0)\to 1$, $f(z_0)\to 1$, and $\mathcal{E}_j(z_0)\to 1$ in the limit of zero z_0. We also considered the relation $G_5 = \pi/N_c^2$, where N_c is the number of colors. It is instructive to write an explicit expression for $\mathcal{E}_j(z)$ which is obtained from the transformations

$$\mathcal{E}_j(z) = \left(\frac{\zeta}{f}\right)^{1/2}\left(\frac{\omega^2-q^2g}{\omega^2-q^2}\right)^{\frac{1}{2}\delta_{jx^3}}\left(\psi_j^{(2)} + \frac{\mathcal{B}_j^{(-)}}{\mathcal{A}_j^{(-)}}\psi_j^{(1)}\right), \tag{48}$$

where we have considered $E_j^{(-)}(k) = (\omega^2 - q^2)^{\frac{1}{2}\delta_{jx^3}} \mathcal{A}_j^{(-)}(k)$ in order to guarantee the condition $\mathcal{E}_j(0) = 1$. Plugging (48) in (47a) and (47b), and using also (36a) and (36b), we get

$$C^R_{x^3x^3}(\omega,q) = -\frac{N_c^2}{8\pi^2}\left(\frac{\omega^2}{\omega^2-q^2}\right) \times \lim_{z_0\to 0}\left(\frac{c}{2}+d+2d\ln z_0+\frac{\mathcal{B}^{(-)}_{x^3}(\omega,q)}{\mathcal{A}^{(-)}_{x^3}(\omega,q)}+\cdots\right), \tag{49a}$$

$$C^R_{\alpha\alpha}(\omega,q) = -\frac{N_c^2}{8\pi^2}\lim_{z_0\to 0}\left(\frac{c}{2}+d+2d\ln z_0 + \frac{\mathcal{B}^{(-)}_{\alpha}(\omega,q)}{\mathcal{A}^{(-)}_{\alpha}(\omega,q)}+\cdots\right); \tag{49b}$$

the ellipses represent terms which are zero in the limit of zero z_0. We rule out the divergent terms, i.e., $\ln z_0$, adding appropriate counterterms in the action (17). Thus, one may calculate the spectral functions, which are defined as the imaginary part of the retarded Green's functions

$$\mathcal{R}_{x^3x^3}(\omega,q) \equiv -2\mathrm{Im}C^R_{x^3x^3}(\omega,q) = \frac{N_c^2}{4\pi^2}\left(\frac{\omega^2}{\omega^2-q^2}\right)\mathrm{Im}\left[\frac{\mathcal{B}^{(-)}_{x^3}(\omega,q)}{\mathcal{A}^{(-)}_{x^3}(\omega,q)}\right], \tag{50a}$$

$$\mathcal{R}_{\alpha\alpha}(\omega,q) \equiv -2\mathrm{Im}C^R_{\alpha\alpha}(\omega,q) = \frac{N_c^2}{4\pi^2}\mathrm{Im}\left[\frac{\mathcal{B}^{(-)}_{\alpha}(\omega,q)}{\mathcal{A}^{(-)}_{\alpha}(\omega,q)}\right]. \tag{50b}$$

As can be seen, the spectral functions depend on the ratio $\mathcal{B}_j^{(-)}/\mathcal{A}_j^{(-)}$ which are the coefficients related to the ingoing solution. One may rewrite this relation in terms of the normalizable and non-normalizable solutions using the matrix relation (40) (for additional details, see Refs. [22,23]),

$$\frac{\mathcal{B}_j^{(-)}}{\mathcal{A}_j^{(-)}} = -\frac{\partial_z\psi_j^{(-)}\psi_j^{(2)} - \psi_j^{(-)}\partial_z\psi_j^{(2)}}{\partial_z\psi_j^{(-)}\psi_j^{(1)} - \psi_j^{(-)}\partial_z\psi_j^{(1)}}. \tag{51}$$

In the following, our strategy shall be the following, We solve the differential Eqs. (27) and (30), integrating from the boundary to the horizon using as "initial conditions" the asymptotic solutions (36a) and (36b). Then, we plug these solutions into (51), evaluate them at the horizon, and finally extract the imaginary part to get the retarded Green's function.

In the sequence, we present our results for the spectral functions computed following the previous procedure. These results are closely related to the results displayed in Fig. 2. For $\mu = 0$, we obtained two branches for the temperature, large and small black holes. The former is a stable phase from the thermodynamic point of view, while the last is unstable. If we investigate the melting at zero chemical potential, we realized that solutions are only possible for temperatures larger than the global minimum, $T \geq 0.612$ GeV. As can be seen in the figure of the potential, see blue line in Fig. 5, there is no potential well for this temperature. This means that no peaks are expected in the spectral functions, meaning that the quasiparticles were dissociated.

On the other hand, from Fig. 2, we realized that the only way to reach low temperatures is to turn on the chemical potential. To be more specific, for $0 < \mu < \mu_c$, it is possible to get three phases for the same temperature; see the left panel of Fig. 2 for $\mu = 0.2$ GeV. In the following, we work on the third branch where we can reach low temperatures. For $\mu = 0.2$ GeV, the temperature in this branch belongs to the interval $0 \leq T \leq 0.936$ GeV. Our numerical results for the spectral function for $q = 0$ and selected values of the temperature are displayed in Fig. 6 considering different scales. The locations of the peaks on the horizontal axis are interpreted as the mass of the quasiparticle states (which also corresponds to the real part of the frequency), while the widths of the peaks are related to the inverse of the decay rate of these quasiparticle states (related to the imaginary part of the frequency). As can be seen in the left panel, the

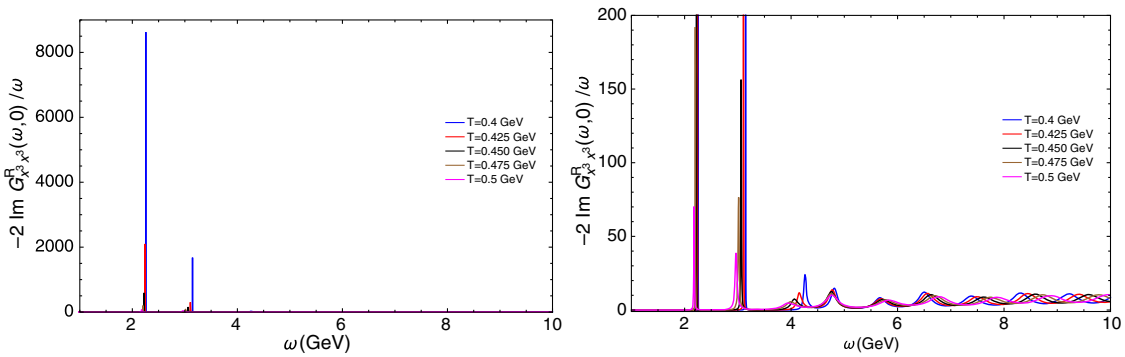

FIG. 6. The spectral function for $\mu = 0.2$ GeV and selected values of the temperature and $q = 0$.

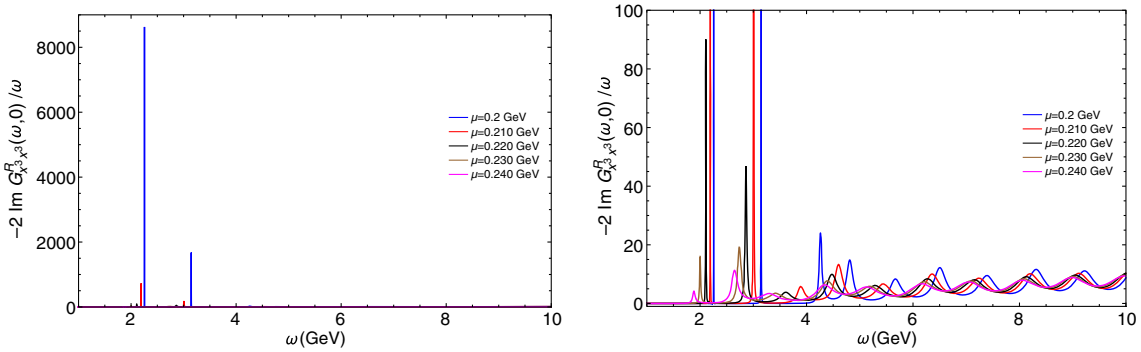

FIG. 7. The spectral function for $T = 0.4$ GeV and selected values of the chemical potential and $q = 0$.

height of the peaks decreases with the increasing of the temperature, while the width of the peaks increases, meaning that the decay time decreases; i.e., the quasiparticles melt faster when the temperature increases. These results are in agreement with previous results obtained in the literature; see, for instance, Refs. [22,23,33,34]. It is worth mentioning that the background metric considered in those holographic models is always AdS, while in the model we are working with, the metric is asymptotically AdS. Recently, a background obtained solving the Einstein-Maxwell-dilaton equations was investigated in Ref. [62]. On the left panel of Fig. 6, we chose a vertical scale such that the highest peak, corresponding to the first radial excitation, is shown in his total height. This way one can see the relative sizes of the peaks. On the other hand, in the right panel of the same figure, we display the spectral function in an expanded scale, such that one can notice the presence of a series of additional peaks arising in the spectral function, corresponding to the higher-order excited states. This means that the model we consider is capable, through numerical methods, of studying high-order excitations of charmonium not previously studied in the literature. From Fig. 6, we conclude that at temperatures larger than the confinement/deconfinement temperature, 0.170 GeV, we still have the presence of charmonium states in the quark-gluon plasma. This result is in agreement with previous results in the literature indicating that heavy vector mesons melt at temperatures above 0.170 GeV; see, for instance, Refs. [32,33].

Now, we investigate the effects of the density on the spectral functions. For this analysis, we fix the temperature at $T = 0.4$ GeV and compute the spectral functions for selected values of the chemical potential. Our numerical results are displayed in Fig. 7 considering different scales. As can be seen in the left panel, the chemical potential speeds up the melting process because the height of the peaks decreases rapidly, and the widths of the peaks increase; see right panel. We also realize that increasing the chemical potential produces a stronger dissociation effect on the quasiparticles than increasing the temperature by the same amount. The right panel also shows the additional peaks arising due to the sensitivity of the numerical procedure. These results are in agreement with previous results in the literature where holographic models for investigating the melting of particles including finite density effects were investigated [34,35].

Finally, it should be interesting to see the spectral function at the critical end point of the phase diagram; see the right panel of Fig. 2. For that reason, we calculate the spectral functions for $\mu = \mu_c$ and selected values of the temperature: $T = 0.534$ GeV, $T = T_c = 0.559$ GeV, and $T = 0.584$ GeV. We display our numerical results in Fig. 8, in which one can see that at the critical end point temperature (red line) the spectral function does not have peaks, meaning that quasiparticles melted. In turn, for temperature lower than the critical one (blue line), the spectral function shows a few peaks, meaning that a few quasiparticles states might be present in the plasma. For a temperature above the critical one (black line), we do not see peaks in the spectral function.

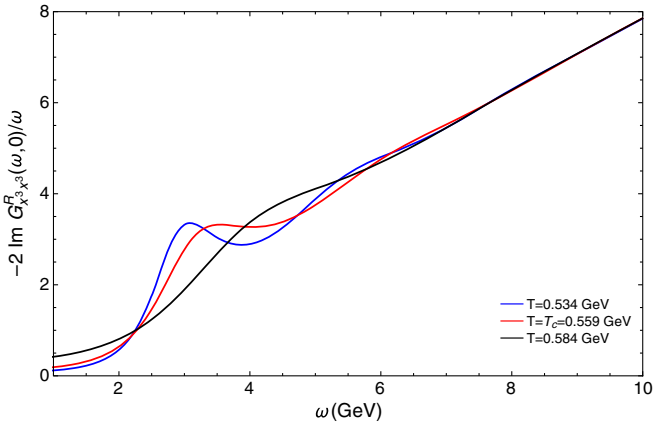

FIG. 8. The spectral function for $\mu = \mu_c = 0.708$ GeV and selected values of the temperature and $q = 0$.

VI. HYDRODYNAMIC LIMIT

In the long-wave and low-energy regime, the theory can be described by an effective hydrodynamic description; in this regime, one may investigate important physical properties of the system like transport properties. The gauge/gravity duality provides us the theoretical framework to investigate this regime in the dual field theory by solving the perturbation equations, arising in the gravitational side, in the hydrodynamic limit. These perturbations are characterized by a set of complex frequencies, the quasinormal modes, which in the hydrodynamic limit are known as hydrodynamic quasinormal modes.

A. Longitudinal sector

As described in previous sections, longitudinal perturbation propagating along the direction $k^\mu = (\omega, 0, 0, q)$ is described by Eq. (26). In this section, we are going to solve this equation in the hydrodynamic limit; for doing so, it is convenient to normalize the parameters by the temperature such that the new parameters and the holographic coordinate become dimensionless:

$$\mathfrak{w} = \frac{\omega}{\pi T}, \qquad \mathfrak{q} = \frac{q}{\pi T}, \qquad \mathfrak{u} = \frac{\mu}{\pi T},$$
$$\mathfrak{c} = \frac{c}{(\pi T)^2}, \qquad \mathfrak{b} = \frac{b}{(\pi T)^4}, \qquad u = (\pi T) z. \tag{52}$$

Then, the dimensionless version of Eq. (26b) is given by

$$E''_{x^3}(u) - \left(\frac{(1+2\mathfrak{c}u^2)g(\mathfrak{w}^2-\mathfrak{q}^2 g) - \mathfrak{w}^2 u g'(u)}{u g(\mathfrak{w}^2-\mathfrak{q}^2 g)}\right) E'_{x^3}(u) + \frac{(\mathfrak{w}^2-\mathfrak{q}^2 g)}{g^2} E_{x^3}(u) = 0. \tag{53}$$

Let us consider a transformation which takes into account the ingoing boundary condition at the horizon

$$E_{x^3}(u) = g^{-\frac{i\mathfrak{w}}{4}} F_{x^3}(u), \tag{54}$$

where $F_{x^3}(u)$ is a regular function; then, the differential equation we must solve is

$$F''_{x^3}(u) + \left(\frac{\mathfrak{w}^2 g'(u)}{g(\mathfrak{w}^2-\mathfrak{q}^2 g)} - \frac{1}{u} - 2\mathfrak{c}u - \frac{i\mathfrak{w}g'(u)}{2g}\right) F'_{x^3}(u) + \left(\frac{\mathfrak{w}^2}{g^2} - \frac{\mathfrak{q}^2}{g} + \frac{i\mathfrak{w}g'(u)}{4ug} + \frac{i\mathfrak{c}\mathfrak{w}u g'(u)}{2g} + \frac{i\mathfrak{w}g'(u)^2}{4g^2} - \frac{\mathfrak{w}^2 g'(u)^2}{16 g^2} - \frac{i\mathfrak{w}^3 g'(u)^2}{4g^2(\mathfrak{w}^2-\mathfrak{q}^2 g)} - \frac{i\mathfrak{w}g''(u)}{4g}\right) F_{x^3}(u) = 0. \tag{55}$$

In the hydrodynamic limit, the energy and wave number are smaller than the temperature such that $\mathfrak{w} \ll 1$ and $\mathfrak{q} \ll 1$. Thus, we may build a multiscale perturbative solution on these parameters. Nevertheless, here we will use an alternative expansion considering the new parametrization $\mathfrak{w} \to \lambda\mathfrak{w}$ and $\mathfrak{q} \to \lambda\mathfrak{q}$ such that $\lambda \ll 1$. Then, we use λ as the parameter controlling the expansion,

$$F_{x^3}(u) = F^{(0)}_{x^3} + \lambda F^{(1)}_{x^3}(u) + \lambda^2 F^{(2)}_{x^3}(u) + \cdots. \tag{56}$$

Plugging (56) into (55), we get differential equations for $F^{(0)}_{x^3}$, $F^{(1)}_{x^3}$, and so on. We must solve these differential equations and fix the integration constants imposing regularity conditions at the horizon; at the end, we get the solutions

$$F^{(0)}_{x^3} = F_0, \tag{57a}$$

$$F^{(1)}_{x^3} = \frac{iF_0\mathfrak{w}}{4}\ln[g(u)] + \frac{iF_0\mathfrak{q}^2}{8\mathfrak{w}\mathfrak{c}}\frac{(e^{\mathfrak{c}u^2} - e^{\mathfrak{c}u_h^2})}{\int_0^{u_h}\frac{e^{\mathfrak{c}x^2}x}{g(x)}dx}\ln[g(u)] - \frac{iF_0\mathfrak{w}}{4}\ln[g(u_h)]\frac{\int_0^u \frac{e^{\mathfrak{c}x^2}x}{g(x)}dx}{\int_0^{u_h}\frac{e^{\mathfrak{c}y^2}y}{g(y)}dy}, \tag{57b}$$

where F_0 is a constant. Calculating the dispersion relation is enough to solve up to $F^{(1)}_{x^3}$. Thus, plugging into (54) and imposing the Dirichlet condition at the boundary $E_{x^3}(0) = 0$, we get the dispersion relation

$$\mathfrak{w} = i\frac{(e^{\mathfrak{c}u_h^2}-1)}{8\mathfrak{c}}\left[\frac{\ln g(u_h)}{\int_0^{u_h}\frac{e^{\mathfrak{c}x^2}x}{g(x)}dx}\right]\mathfrak{q}^2. \tag{58}$$

Note that the logarithm and integral blow up at the horizon,

$$\lim_{u\to u_h}\ln g(u) = -\infty, \qquad \lim_{u\to u_h}\int_0^u \frac{e^{\mathfrak{c}x^2}x}{g(x)}dx = \infty. \tag{59}$$

However, one may use l'Hôpital's rule to evaluate this ratio, such that the result is finite,

$$\frac{\ln g(u_h)}{\int_0^{u_h}\frac{e^{\mathfrak{c}x^2}x}{g(x)}dx} = \frac{e^{-\mathfrak{c}u_h^2}g'(u_h)}{u_h}, \;\to\; \mathfrak{w} = i\frac{(e^{\mathfrak{c}u_h^2}-1)}{8\mathfrak{c}}\frac{e^{-\mathfrak{c}u_h^2}g'(u_h)}{u_h}\mathfrak{q}^2. \tag{60}$$

Plugging this result into (58) and considering the definition of the temperature $g'(u_h) = -4$, one gets the dispersion relation

$$\omega = -i\frac{(1-e^{-\mathfrak{c}u_h^2})}{2\mathfrak{c}u_h(\pi T)}q^2. \tag{61}$$

Result (60) represents the most general solution for this kind of holographic models. For a check of consistency, let us apply this formula for problems investigated previously in the literature. Considering $g(u) = 1-u^4$ and $u_h = 1$, we get Eq. (4.16) of Ref. [63]. In turn, for the problem investigated in Ref. [23], plugging the horizon function $g(u) = 1-u^4$ and $u_h = 1$ into (60), we get the same result obtained in Eq. (4.6) of that paper. For the last check of consistency, we get Eq. (3.31) of Ref. [64], where $g(u) = (1-u)(1+u-(2-4\pi Tb)u^2)$. Applying this formula in our case, we can write the dispersion relation as

$$i\omega = Dq^2, \tag{62}$$

where the coefficient D is given by

$$D = \frac{(1-e^{-\mathfrak{c}u_h^2})}{2\mathfrak{c}u_h(\pi T)}. \tag{63}$$

Meanwhile, following Ref. [63], one may rewrite the field component $E_{x^3}(k,u)$ given by (54) close to the boundary in the form

$$E_{x^3}(u) = \mathfrak{A}_{x^3}(\mathfrak{w},\mathfrak{q}) + \cdots \mathfrak{B}_{x^3}(\mathfrak{w},\mathfrak{q})u^2 + \cdots, \tag{64}$$

where the coefficients are given by

$$\mathfrak{A}_{x^3}(\mathfrak{w},\mathfrak{q}) = F_0\left(1 - i\mathfrak{q}^2\frac{(1-e^{-\mathfrak{c}u_h^2})}{8\mathfrak{c}\mathfrak{w}}\frac{g'(u_h)}{u_h}\right), \tag{65a}$$

$$\mathfrak{B}_{x^3}(\mathfrak{w},\mathfrak{q}) = iF_0\frac{(\mathfrak{q}^2-\mathfrak{w}^2)}{8\mathfrak{w}}\frac{e^{-\mathfrak{c}u_h^2}g'(u_h)}{u_h}. \tag{65b}$$

To write the last expressions, we have used l'Hôpital's rule again. Thus, one may calculate the retarded Green's function from (43). Considering the decomposition of $E_{x^3}(u) = E^{(0)}_{x^3}(k)\mathcal{E}_{x^3}(u)$, from (64), we get [setting $E^{(0)}_{x^3}(k) = \mathfrak{A}_{x^3}(k)$]

$$\mathcal{E}_{x^3}(u) = 1 + \cdots\frac{\mathfrak{B}_{x^3}(\mathfrak{w},\mathfrak{q})}{\mathfrak{A}_{x^3}(\mathfrak{w},\mathfrak{q})}u^2 + \cdots \tag{66}$$

Thus, the correlation functions may be calculated using the functional derivative of the action (43). We have special interest in the component $C^R_{tt}(\mathfrak{w},\mathfrak{q})$, which is given by

$$C^R_{tt}(\mathfrak{w},\mathfrak{q}) = \frac{\delta^2 S}{\delta A^{(0)}_t(k)\delta A^{(0)}_t(-k)} = \frac{\mathfrak{q}^2\delta S}{\delta E^{(0)}_{x^3}(k)\delta E^{(0)}_{x^3}(-k)}. \tag{67}$$

Plugging (66) into the on-shell action and taking the limit $u \to 0$, we rewrite the correlation function in the form depending on the coefficients of the asymptotic expansion close to the boundary,

$$C^R_{tt}(\mathfrak{w},\mathfrak{q}) = \frac{N_c^2}{8\pi^2}\frac{q^2(\pi T)^2}{(q^2-\omega^2)}\frac{\mathfrak{B}_{x^3}(\mathfrak{w},\mathfrak{q})}{\mathfrak{A}_{x^3}(\mathfrak{w},\mathfrak{q})}. \tag{68}$$

Finally, by plugging (65) into the last equation, one gets

$$C^R_{tt}(\omega,q) = \frac{N_c^2}{16\pi^2}\frac{q^2}{z_h}\frac{e^{-cz_h^2}}{(i\omega - q^2\frac{(1-e^{-cz_h^2})}{2cz_h})}. \tag{69}$$

Note that the correlation function has a singular point when the denominator is zero, resulting in the dispersion relation obtained by imposing the Dirichlet boundary condition on the field component $E_{x^3}(u)$; see Eq. (61).

B. Transversal perturbation

The dimensionless version of the transverse sector is given by Eq. (26a), which in dimensionless parameters is given by

$$E''_\alpha(u) - \left(\frac{g'(u)}{g(u)} + \frac{1}{u} - 2\mathfrak{c}u\right)E'_\alpha(u) + \frac{(\mathfrak{w}^2-\mathfrak{q}^2 g)}{g^2}E_\alpha(u) = 0, \quad (\alpha = x^1, x^2). \tag{70}$$

Once again, we consider the transformation which takes into account the ingoing boundary condition at the horizon,

$$E_\alpha(u) = g^{-\frac{i\mathfrak{w}}{4}}F_\alpha(u); \tag{71}$$

generating the differential equation, we must solve

$$F''_\alpha(u) + \left(\frac{g'(u)}{g(u)} - \frac{1}{u} - 2\mathfrak{c}u - \frac{i\mathfrak{w}g'(u)}{2g}\right)F'_\alpha(u) + \left(\frac{\mathfrak{w}^2}{g^2} - \frac{\mathfrak{q}^2}{g} + \frac{i\mathfrak{w}g'(u)}{4ug} + \frac{i\mathfrak{c}\mathfrak{w}ug'(u)}{2g} - \frac{\mathfrak{w}^2g'(u)^2}{16g^2} - \frac{i\mathfrak{w}g''(u)}{4g}\right)F_\alpha(u) = 0. \tag{72}$$

As before, we build the perturbation solution which is controlled by the parameter $\lambda \ll 1$. Thus, we expand F_α in the form

$$F_\alpha(u) = F^{(0)}_\alpha + \lambda F^{(1)}_\alpha(u) + \lambda^2 F^{(2)}_\alpha(u) + \cdots. \tag{73}$$

Plugging (73) into (72) and solving order by order, we get the solutions

$$F_\alpha^{(0)} = F_0, \tag{74a}$$

$$F_\alpha^{(1)} = \frac{iF_0\mathfrak{w}}{4}\ln[g(u)] - \frac{iF_0\mathfrak{w}}{4}\ln[g(u_h)]\frac{\int_0^u \frac{e^{cx^2}x}{g(x)}dx}{\int_0^{u_h}\frac{e^{cy^2}y}{g(y)}dy}. \tag{74b}$$

Calculating the dispersion relation is enough to solve up to $F_\alpha^{(1)}$. Thus, plugging into (71) and imposing the Dirichlet condition at the boundary, $E_\alpha(0) = 0$, we do not get solutions in the hydrodynamic limit, i.e., $\mathfrak{w} \ll 1$ and $\mathfrak{q} \ll 1$. This means that the correlation function does not have poles. It is not difficult to show this statement by expanding the solution, Eq. (71), close to the boundary,

$$E_\alpha(u) = \mathfrak{A}_\alpha(\mathfrak{w},\mathfrak{q}) + \cdots \mathfrak{B}_\alpha(\mathfrak{w},\mathfrak{q})u^2 + \cdots, \tag{75}$$

where the coefficients are given by

$$\mathfrak{A}_\alpha(\mathfrak{w},\mathfrak{q}) = F_0, \tag{76a}$$

$$\mathfrak{B}_\alpha(\mathfrak{w},\mathfrak{q}) = -iF_0\frac{\mathfrak{w}}{8}\frac{e^{-cu_h^2}g'(u_h)}{u_h}. \tag{76b}$$

To write the last expression, we have used l'Hôpital's rule. Thus, one may calculate the retarded Green's function from (43) and the fact that (75) may be decomposed as $E_\alpha(u) = E_\alpha^{(0)}(k)\mathcal{E}_\alpha(u)$, where

$$\mathcal{E}_\alpha(u) = 1 + \cdots\frac{\mathfrak{B}_\alpha(\mathfrak{w},\mathfrak{q})}{\mathfrak{A}_\alpha(\mathfrak{w},\mathfrak{q})}u^2 + \cdots. \tag{77}$$

Thus, the correlation functions may be calculated using the functional derivative of the action (43). We are interested in the component $C^R_{\alpha\alpha}(\mathfrak{w},\mathfrak{q})$, which is given by

$$C^R_{\alpha\alpha}(\mathfrak{w},\mathfrak{q}) = \frac{\delta^2 S}{\delta A_\alpha^{(0)}(k)\delta A_\alpha^{(0)}(-k)} = \frac{\mathfrak{w}^2\delta S}{\delta E_\alpha^{(0)}(k)\delta E_\alpha^{(0)}(-k)}. \tag{78}$$

Plugging (77) into the on-shell action and taking the limit $u \to 0$, we rewrite the correlation function in the form depending on the coefficients of the asymptotic expansion close to the boundary,

$$C^R_{\alpha\alpha}(\mathfrak{w},\mathfrak{q}) = -\frac{N_c^2T^2}{8}\frac{\mathfrak{B}_\alpha(\omega,q)}{\mathfrak{A}_\alpha(\omega,q)}. \tag{79}$$

Finally, by plugging (76) into the last equation, one gets

$$C^R_{\alpha\alpha}(\omega,q) = -\frac{N_c^2}{16\pi^2}\frac{i\omega e^{-cz_h^2}}{z_h}. \tag{80}$$

Note that the correlation function has no poles, which is consistent with the solution in the hydrodynamic limit.

VII. QUARK NUMBER SUSCEPTIBILITY

In QCD, the response of the system to a change in the chemical potential is measured through the quark number susceptibility χ, and it was investigated in holographic QCD models in Refs. [48,64–68] (see also references therein). Once we have solved the differential equations in the hydrodynamic limit and obtained the retarded Green's functions, we can then calculate the quark number susceptibility following the procedure implemented in Refs. [64,65], where they used the prescription

$$\chi(T,\mu) = -\lim_{q\to 0}\mathrm{Re}\{C_{tt}(0,q)\}. \tag{81}$$

Thus, from (69), we get

$$\frac{\chi(T,\mu)}{N_c^2} = \frac{1}{8\pi^2}\frac{c}{(e^{cz_h^2}-1)}. \tag{82}$$

Note that, even though this result is similar to the one obtained in Refs. [48,64], the model we are working with has an additional parameter b and an intricate form for the horizon function $g(z)$. In turn, one may compare this result against the one obtained using the baryon density read off from Eqs. (7) and (13), which is given by [46]

$$\rho = \frac{c\mu}{e^{cz_h^2}-1}. \tag{83}$$

Then, we calculate the quark number susceptibility

$$\chi = \frac{\partial\rho}{\partial\mu} = \frac{c}{e^{cz_h^2}-1} - \frac{2c^2\mu z_h e^{cz_h^2}}{(e^{cz_h^2}-1)^2}\frac{1}{\partial_{z_h}\mu}. \tag{84}$$

Let us calculate the behavior of Eqs. (82) and (84) in the conformal limit, i.e., high-temperature regime, where we get the relation $z_h = 1/(\pi T)$ (see the left panel of Fig. 2). Plugging this result in (82) and (83), then, considering the approximation $e^{c/(\pi T)^2} \approx 1 + c/(\pi T)^2$, we get

$$\chi = \frac{N_c^2}{8}T^2 \quad \text{and} \quad \chi = \pi^2T^2, \tag{85}$$

respectively. This result is in agreement with the result found in the literature; see, for instance, Refs. [64,66,67], where the quark number susceptibility goes like $\chi \sim T^2$. Let us plot Eqs. (82) and (84) as a function of the chemical potential for selected values of the temperature. Our numerical results are displayed in Fig. 9, in which the left panel shows Eq. (82) while right panel shows the results for Eq. (84). It is worth mentioning that previous investigation works showed that the quark susceptibility

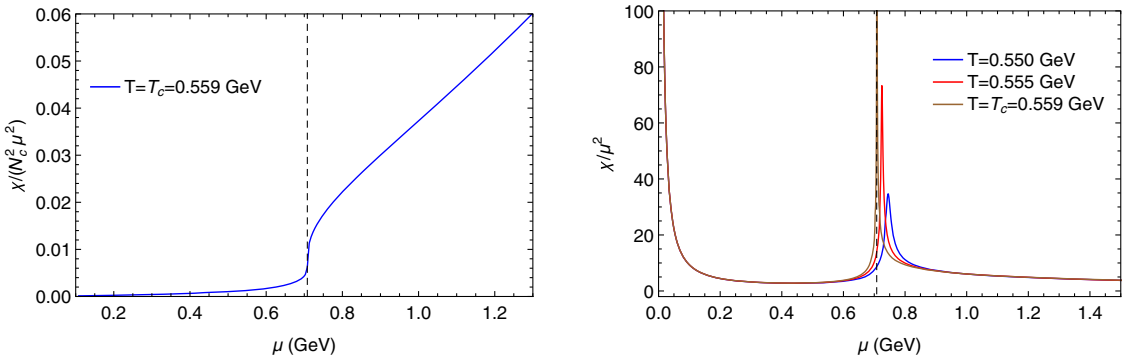

FIG. 9. Left: the quark number susceptibility as a function of the chemical potential for $T = T_c = 0.599$ GeV given by Eq. (82). Right: the quark number susceptibility as a function of the chemical potential for $T = 0.550$ GeV (blue), $T = 0.555$ GeV (red), and $T = 0.559$ GeV (brown) given by Eq. (84). Both panels also show the critical value for the chemical potential represented by the vertical dashed line.

must blow up at the critical end point; for results obtained solving the Dyson-Schwinger equation, see Ref. [69] and references therein. Our results are showing two different behaviors for the quark number susceptibility, one obtained from Eq. (82) and another from Eq. (84). The result displayed in the left panel of Fig. 9 does not diverge at the critical end point. This result may be explained because the matter action we are considering to get Eq. (82) represents the action of probe fields. In the dual field theory, this corresponds to the quenched approximation [57]. In turn, the right panel of Fig. 9 shows that χ blows up at the critical end point. Note that Eq. (84) was obtained using the holographic dictionary on A_t, which was obtained by solving Maxwell's equations (5). It is also worth mentioning that the holographic model we are working with was obtained solving differential equations numerically. This means that we have numerical error. We made an estimate of the error order, which is $\sim 10^{-8}$ close to the boundary. Therefore, we present a qualitative instead of quantitative comparison against results available from the lattice and experimental measurement [70–72]. Certainly, this point can be better explored in future works.

VIII. QUASINORMAL MODES

In this section, we calculate the quasinormal frequencies by solving the differential equations numerically. We split up the problem in two parts: the longitudinal and the transverse sectors. To calculate the quasinormal frequencies, we are going to use the pseudospectral method; for a discussion, see Ref. [73], and see also Refs. [25,74–77] and references therein, where the pseudospectral method was applied to calculate quasinormal frequencies in different scenarios.

A. Longitudinal sector

Our starting point is the Schrödinger-like equation (30), with potential (32). From here on, we follow the procedure implemented in Ref. [77]. To write the differential equation suitable to apply the pseudospectral method, we first implement the transformation $\psi_\alpha = e^{-i\omega r_*}\varphi$. Then, we replace the tortoise coordinate and B_L to get

$$(4q^2z^2\omega^4 - 8q^4z^2\omega^2 g + 3\omega^4 g + 4c^2z^4\omega^4 + 4q^6z^2g^2 - 6q^2\omega^2g^2 - 8c^2q^2z^4\omega^2g^2 + 3q^4g^3 + 4c^2q^4z^4g^3 - 2z\omega^4 g' - 4cz^3\omega^4 g' + 2q^2z\omega^2 gg' + 4cq^2z^3\omega^2 gg' + 2q^2z^2\omega^2 g'^2 + q^4z^2gg'^2 + 2q^2z^2\omega^2 gg'' - 2q^4z^2g^2g'')\varphi(z) - (8iz^2\omega(\omega^2 - q^2g)^2 + 4z^2(\omega^2 - q^2g)^2 g')\varphi'(z) - g(4z^2\omega^4 - 8q^2z^2\omega^2 g + 4q^4z^2g^2)\varphi''(z) = 0. \quad (86)$$

To compare our results against the results obtained in Ref. [63], for $\mu = 0$, and $c = 0 = b$, we normalize the coordinate and parameters by the temperature

$$u = z\pi T; \qquad \tilde{\omega} = \frac{\omega}{2\pi T}; \qquad \tilde{q} = \frac{q}{2\pi T}; \qquad \tilde{c} = \frac{c}{(\pi T)^2}; \qquad \tilde{b} = \frac{b}{(\pi T)^4}; \qquad \tilde{\mu} = \frac{\mu}{\pi T}. \quad (87)$$

One may calculate the asymptotic solutions of the last differential equation close to the horizon considering the ansatz $\varphi \sim (1-u)^{\alpha}$. Plugging in Eq. (86), we get

$$\alpha_1 = 0, \qquad \alpha_2 = 4i\tilde{\omega}. \tag{88}$$

The first solution is interpreted as the ingoing solution, falling into the black hole event horizon, while the second solution is interpreted as the outgoing solution. As we are interested in retarded Green's functions, we choose the ingoing solution in the following analysis. In turn, to calculate the asymptotic solution close to the boundary, we consider the ansatz $\varphi \sim u^{\beta}$. Plugging in (86), we get the solutions

$$\beta_1 = -\frac{1}{2}, \qquad \beta_2 = \frac{3}{2}, \tag{89}$$

where the first solution is interpreted as the nonnormalizable solution while the second the normalizable one. As we are looking for normalizable solutions of the eigenvalue problem, we consider the normalizable solution in the following analysis. Then, to get the final differential equation to solve, we consider the additional transformation, which takes into account the information about the asymptotic solutions we got, $\varphi(u) = u^{3/2}\phi(u)$,

$$\begin{aligned}&(8(2\tilde{q}^2u - 3i\tilde{\omega})\tilde{\omega}^4 + 4\tilde{c}^2\tilde{q}^4u^3g^3 - 4(2+\tilde{c}u^2)\tilde{\omega}^4g' + 2\tilde{q}^2u\tilde{\omega}^2g'^2 + 2g^2(8\tilde{q}^6u - 12i\tilde{q}^4\tilde{\omega} - 4\tilde{c}^2\tilde{q}^2u^3\tilde{\omega}^2 - 3\tilde{q}^4g' - \tilde{q}^4ug'')\\ &\quad + g(2\tilde{\omega}^2(-16\tilde{q}^4u + 24i\tilde{q}^2\tilde{\omega} + 2\tilde{c}^2u^3\tilde{\omega}^2 + \tilde{q}^2ug'') + 2\tilde{q}^2(7+2\tilde{c}u^2)\tilde{\omega}^2g' + \tilde{q}^4ug'^2))\phi(u)\\ &\quad - 4i(\tilde{\omega}^2 - \tilde{q}^2g)^2(4u\tilde{\omega} - 3ig - iug')\phi'(u) - 4ug(\tilde{\omega}^2 - \tilde{k}^2g)^2\phi''(u) = 0.\end{aligned} \tag{90}$$

As can be seen, we get an eigenvalue problem on the frequency, to solve it we are going to use the pseudospectral method. Nevertheless, in the holographic model, we are working with three parameters: μ, c, and b. To see how the quasinormal (QN) frequencies change with the chemical potential $\tilde{\mu}$, we set $\tilde{c} = 0 = \tilde{b}$. It is worth mentioning that in this case the horizon function reduces to the Reissner-Nordström AdS solution

$$g = 1 - \left(1 + \frac{\tilde{\mu}^2}{3}\right)u^4 + \frac{\tilde{\mu}^2}{3}u^6. \tag{91}$$

One of the zeros of the equation $g(u) = (u^2 - u_1)(u^2 - u_2)(u^2 - u_3) = 0$ represents the location of the event horizon, which we fix at $u_h = 1$ due to the normalization we are working with (87). Then, the solutions are

$$u_1^2 = 1, \quad u_2^2 = \frac{3 - \sqrt{9 + 12\tilde{\mu}^2}}{2\tilde{\mu}^2}, \quad u_3^2 = \frac{3 + \sqrt{9 + 12\tilde{\mu}^2}}{2\tilde{\mu}^2}. \tag{92}$$

As can be seen, u_1^2 does not depend on the chemical potential, while u_2^2 is always negative for $\tilde{\mu} > 0$. Meanwhile, $u_3^2 > 1$ for $\tilde{\mu} > 0$, while it becomes $u_3^2 = 1$ for $\tilde{\mu} = \sqrt{6}$, and $u_3^2 < 1$ for $\tilde{\mu} > \sqrt{6}$. For that reason, we restrict our numerical analysis to the region where $\tilde{\mu} \leq \sqrt{6}$. This means that the horizon lies at $u_h = 1$.

Our numerical results for $\tilde{q} = 1$ are displayed in Table II. We point out that the results for $\tilde{\mu} = 0$ are in agreement with those results obtained in Ref. [63]. As can be seen, the real part of the frequency decreases with the increasing of the chemical potential in the region of small values for the chemical potential; then, it increases with the increasing of

TABLE II. The quasinormal frequencies of the longitudinal sector for selected values of the chemical potential for $\tilde{q} = 1$, $\tilde{c} = 0$, and $\tilde{b} = 0$. The results for $\tilde{\mu} = 0$ are equivalent to those of Ref. [63].

n	$\tilde{\mu} = 0$	$\tilde{\mu} = 0.01$	$\tilde{\mu} = 0.1$
0	$\pm 1.1478314 - 0.5592036i$	$\pm 1.1478256 - 0.5592051i$	$\pm 1.1472503 - 0.5593576i$
1	$\pm 1.9100059 - 1.7580648i$	$\pm 1.9099775 - 1.7580789i$	$\pm 1.9071552 - 1.7594740i$
2	$\pm 2.9032931 - 2.8916809i$	$\pm 2.9032453 - 2.8917233i$	$\pm 2.8984967 - 2.8959528i$
3	$\pm 3.9285553 - 3.9433859i$	$\pm 3.9284951 - 3.9434557i$	$\pm 3.9225172 - 3.9504090i$
4	$\pm 4.9468182 - 4.9651851i$	$\pm 4.9467456 + 4.9652802i$	$\pm 4.9395555 - 4.9747681i$
n	$\tilde{\mu} = 0.2$	$\tilde{\mu} = 0.3$	$\tilde{\mu} = 0.5$
0	$\pm 1.1455051 - 0.5598240i$	$\pm 1.1425904 - 0.5606158i$	$\pm 1.1332155 - 0.5632753i$
1	$\pm 1.8985348 - 1.7637362i$	$\pm 1.8839332 - 1.7709573i$	$\pm 1.8350724 - 1.7950779i$
2	$\pm 2.8839215 - 2.9090645i$	$\pm 2.8589691 - 2.9319886i$	$\pm 2.7723821 - 3.0169965i$
3	$\pm 3.9042584 - 3.9721219i$	$\pm 3.8733809 - 4.0107026i$	$\pm 3.7734185 - 4.1623459i$
4	$\pm 4.9177089 - 5.0045069i$	$\pm 4.8812902 - 5.0577870i$	$\pm 4.7755298 - 5.2719366i$

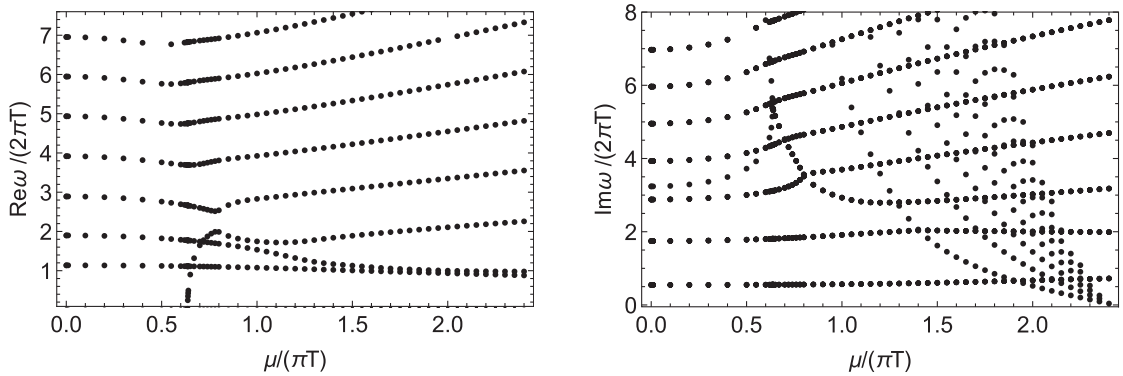

FIG. 10. Left: the real part of the frequency as a function chemical potential. Right: the imaginary part of the frequency as a function of the chemical potential. These results were obtained for $q/(2\pi T) = 1$ and $c = 0 = b$.

the chemical potential. However, the ground and first two states deserve an additional comment. As can be seen in Fig. 10, there is a new mode whose real part starts to grow up at approximately $\tilde{\mu} \approx 0.637$. It grows up rapidly and crosses the ground state; however, it is not clear if this mode crosses or stays below the first state (see the left panel of Fig. 10). In turn, the imaginary part always increases with the increasing of the chemical potential (see the right panel of Fig. 10).

The hydrodynamic frequency has an imaginary part different from zero, $\tilde{\omega} = -3.2506370i$, which is also in agreement with the result of Ref. [63] for $\tilde{\mu} = 0$. The dependence of the hydrodynamic frequency with chemical potential deserves an additional analysis. Our numerical results for this frequency considering selected values of the chemical potential are displayed in Table III. As can be seen, the frequency increases with the increasing of the chemical potential. However, at $\tilde{\mu} \approx 0.637$, it seems that the hydrodynamic mode merges with a new mode coming from above; see the right panel of Fig. 10. It is also worth mentioning that a family of purely imaginary modes shows up in the spectrum. They have a characteristic behavior, decreasing with the increasing of the chemical potential, and are purely imaginary; see the right panel of the same figure. This kind of behavior was previously observed in the literature; see, for instance, Ref. [78] (see also Ref. [79] to see how this kind of mode behaves as a function of the rotation parameter).

TABLE III. The hydrodynamic frequency for different values of the chemical potential. These results were obtained considering $q/(2\pi T) = 1$ and $c = 0 = b$.

$\tilde{\mu} = 0$	$-3.2506370i$
$\tilde{\mu} = 0.01$	$-3.2507627i$
$\tilde{\mu} = 0.1$	$-3.2633614i$
$\tilde{\mu} = 0.2$	$-3.3035845i$
$\tilde{\mu} = 0.3$	$-3.3786204i$
$\tilde{\mu} = 0.5$	$-3.7348719i$
$\tilde{\mu} = 0.6$	$-4.2947702i$
$\tilde{\mu} = 0.62$	$-4.5834402i$

Let us now compare the analytic solution obtained in the hydrodynamic limit, i.e., Eq. (61), against the numerical solution. For $\tilde{\mu} = 0$, we realized that the coefficient $D = \pi T(1 - e^{-cz_h^2})/(cz_h)$ lies close to the unity when $T \geq T_{\min}$ for the big black hole branch; see the blue line in the left panel of Fig. 11. In turn, the coefficient D increases when $T \geq T_{\min}$ for the small black hole branch; see the red line in the left panel of Fig. 11. In turn, for $\mu \geq \mu_c$, the diffusion coefficient becomes zero in the limit of zero temperature; then, it increases, converging to unity in the limit of high temperatures where conformal symmetry must be restored; see the blue line in the same figure. Meanwhile, the results for the dispersion relation are displayed in the right panel of Fig. 11, in which continuous lines represent analytic results for the conformal (black line) and nonconformal case (red line), while numerical solutions for the conformal are represented by dashed black line, and nonconformal are represented by dashed red. In the nonconformal case, we fixed the parameters $\mu = \mu_c$, $c = 1.46\ \text{GeV}^2$, $b = 0.273\ \text{GeV}^4$, and $T = T_c$. As can be seen, in the nonconformal case, the frequency decreases. It is also worth mentioning that the precision of the numerical method gets poor in the nonconformal case.

We also calculated the quasinormal frequencies as a function of the momentum. Our numerical results are displayed in Fig. 12, in which black dots represent the results obtained in the conformal case, while red squares represent the results obtained in the nonconformal case. As can be seen, the real part of the frequency increases when we turn on the parameters, and we also observe that higher states are more sensitive to the parameters than lower states. In turn, the imaginary part decreases when we turn on the parameters; again, higher states are more sensitive to the parameters than lower states.

B. Transverse sector

Our starting point is the Schrödinger-like equation (27), with the potential given by (29). First, we implement the transformation $\psi_\alpha = e^{-i\omega r_*}\varphi$. Then, we replace the tortoise coordinate and B_T to get

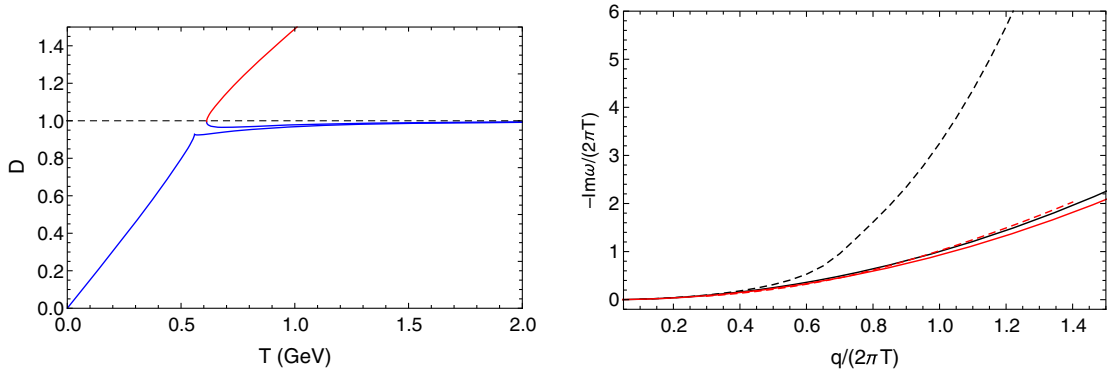

FIG. 11. Left: the diffusion coefficient as a function of the temperature; the colors correspond to the notation used in Fig. 2, and the conformal case is represented by the horizontal dashed line. Right: the numerical (dashed lines) and analytic (solid lines) solutions for the hydrodynamic frequency for $\mu = 0$ and $c = 0 = b$ (black) and for $\mu = \mu_c$, $c = 1.46$ GeV^2, $b = 0.273$ GeV^4, and $T = T_c$ (red).

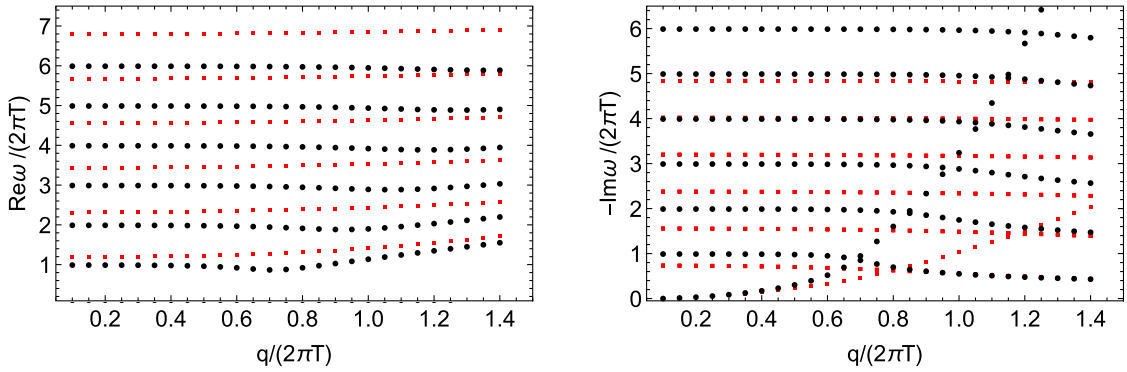

FIG. 12. Left: the real part of the frequency as a function of the wave number. Right: the imaginary part of the frequency as a function of the wave number. Black dots represent the results for $\mu = 0$ and $c = 0 = b$ (conformal case), while red squares were obtained for $\mu = \mu_c$, $c = 1.46$ GeV^2, $b = 0.273$ GeV^4, and $T = T_c$ (nonconformal case).

$$(4q^2z^2 + 3g + 4c^2z^4g - 2zg' - 4cz^3g')\varphi(z) - z^2(8i\omega + 4g')\varphi'(z) - 4z^2g\varphi''(z) = 0. \tag{93}$$

In the following, we normalize the variable and parameters as in (87). To solve the problem numerically, we also need to calculate the asymptotic solutions close to the horizon, $u = 1$. Considering the ansatz $\varphi = (1-u)^\alpha$, then, plugging it in the last equation, we get the solutions

$$\alpha_1 = 0, \qquad \alpha_2 = 4i\tilde{\omega}. \tag{94}$$

The first solution is interpreted as waves falling into the black hole through the event horizon, while the second solution represents waves coming out from the black hole interior. Classically, nothing comes from the black hole interior, and for that reason, we work with the first solution. Then, the solution at the horizon reduces to a constant that we can set to the unit.

Repeating the procedure close to the boundary, $u = 0$, considering the ansatz $\varphi = u^\beta$, plugging into the differential equation, and solving the leading equation, we get the solutions

$$\beta_1 = -\frac{1}{2}, \qquad \beta_2 = \frac{3}{2}. \tag{95}$$

The first solution is interpreted as the non-normalizable (or source), while the second is interpreted as the normalizable [or vacuum expectation value (VEV)]. The QN frequencies are solutions of the differential equation by imposing the Dirichlet condition at the boundary, such that the poles of the retarded Green's functions correspond to the QN frequencies; this means that we must neglect the non-normalizable solution in (95). Thus, the last transformation is given by $\varphi = u^{3/2}\phi(u)$, leading us to the final differential equation

$$(4\tilde{q}^2u - 6i\tilde{\omega} + \tilde{c}^2u^3g - (2 + \tilde{c}u^2)g')\phi(u) - (4i\tilde{\omega}u + 3g + ug')\phi'(u) - ug\phi''(u) = 0. \tag{96}$$

As a check of consistency, let us calculate the QN frequencies setting $\tilde{\mu} = 0$, $\tilde{c} = 0$, and $\tilde{b} = 0$. The problem reduces to the case investigated in Ref. [63]. Our numerical results for the frequencies are displayed in Table IV, for $\tilde{\mu} = 0$. As can be seen, the first four QN frequencies are in

TABLE IV. The quasinormal frequencies for selected values of the chemical potential for $q/(2\pi T) = 1$, $c = 0$, and $b = 0$. The results for $\mu = 0$ are equivalent to those of Ref. [63].

n	$\tilde{\mu} = 0$	$\tilde{\mu} = 0.01$	$\tilde{\mu} = 0.1$
0	$\pm 1.5471870 - 0.8497232i$	$\pm 1.5471814 - 0.8497309i$	$\pm 1.5466297 - 0.8504960i$
1	$\pm 2.3989034 - 1.8743432i$	$\pm 2.3988866 - 1.8743668i$	$\pm 2.3972277 - 1.8767126i$
2	$\pm 3.3232289 - 2.8949008i$	$\pm 3.3231995 - 2.8949440i$	$\pm 3.3202938 - 2.8992378i$
3	$\pm 4.2764313 - 3.9095832i$	$\pm 4.2763887 - 3.9096479i$	$\pm 4.2721793 - 3.9160847i$
4	$\pm 5.2440583 - 4.9203464i$	$\pm 5.2440021 - 4.9204338i$	$\pm 5.2384548 - 4.9291372i$
n	$\tilde{\mu} = 0.2$	$\tilde{\mu} = 0.5$	$\tilde{\mu} = 1$
0	$\pm 1.5449644 - 0.8528302i$	$\pm 1.5336234 - 0.8698423i$	$\pm 1.5010485 - 0.9401700i$
1	$\pm 2.3922258 - 1.8839098i$	$\pm 2.3587417 - 1.9382540i$	$\pm 2.3025258 - 2.1792915i$
2	$\pm 3.3115486 - 2.9124735i$	$\pm 3.2546584 - 3.0154195i$	$\pm 3.2350527 - 3.4380124i$
3	$\pm 4.2595354 - 3.9360044i$	$\pm 4.1803200 - 4.0948307i$	$\pm 4.2135273 - 4.6768033i$
4	$\pm 5.2218242 - 4.9561634i$	$\pm 5.1223650 - 5.1761809i$	$\pm 5.2107958 - 5.9057699i$
n	$\tilde{\mu} = 1.2$	$\tilde{\mu} = 1.5$	$\tilde{\mu} = 2$
0	$\pm 1.4917208 - 0.9860494i$	$\pm 1.4946232 - 1.0638620i$	$\pm 1.5262256 - 1.1876869i$
1	$\pm 2.3258501 - 2.3022563i$	$\pm 2.3822490 - 2.4727024i$	$\pm 2.5070989 - 2.7321848i$
2	$\pm 3.2897756 - 3.6134830i$	$\pm 3.3970290 - 3.8642567i$	$\pm 3.6112874 - 4.2453557i$
3	$\pm 4.2964798 - 4.9072267i$	$\pm 4.4515234 - 5.2357684i$	$\pm 4.7516006 - 5.7369090i$
4	$\pm 5.3214206 - 6.1898699i$	$\pm 5.5227181 - 6.5960159i$	$\pm 5.9070037 - 7.2171368i$

good agreement with the results displayed in the first table of Appendix B in Ref. [63]. In turn, the fifth frequency is in agreement up to the fourth decimal. It is worth pointing out that the results of Ref. [63] were obtained using the Frobenius method.

A plot of the real and imaginary parts of the frequency as a function of the chemical potential is displayed in Fig. 13. As can be seen, the real part decreases in the region of small values of the chemical potential, reaches a minimum, and then increases; see the top-left panel. This behavior is

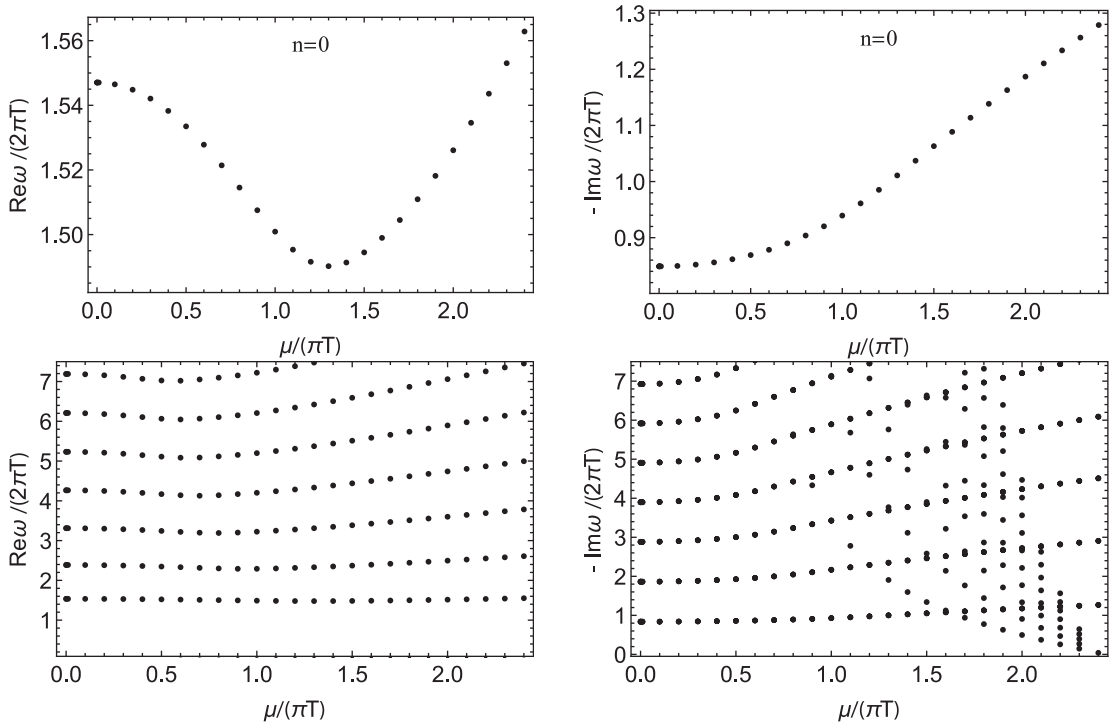

FIG. 13. Left: the real part of the frequency as a function of the chemical potential. Right: the imaginary part of the frequency as a function of the chemical potential. These results were obtained setting $q/(2\pi T) = 1$, and $c = 0 = b$.

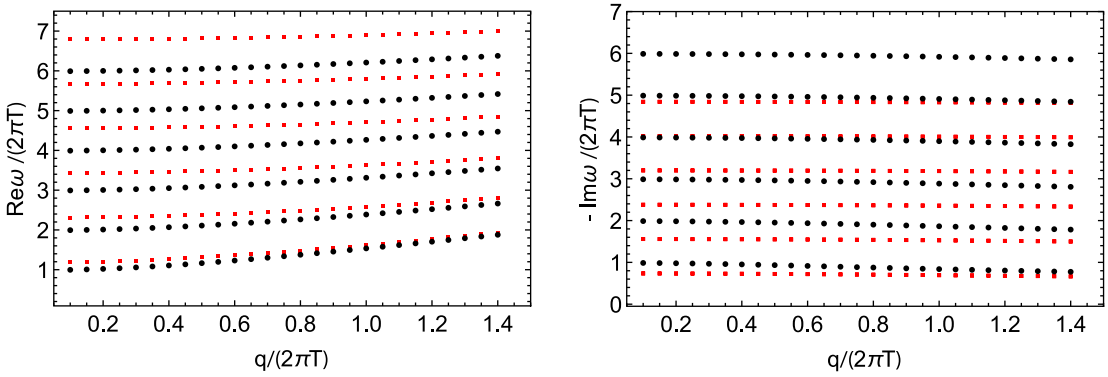

FIG. 14. Left: the real part of the frequency as a function of the wave number. Right: the imaginary part of the frequency as a function of the wave number. Black dots represent the results for $\mu = 0$ and $c = 0 = b$ (conformal case), while red squares were obtained for $\mu = \mu_c$, $c = 1.46\ \mathrm{GeV}^2$, $b = 0.273\ \mathrm{GeV}^4$, and $T = T_c$ (nonconformal case).

shared by the real part of the other quasinormal frequencies. Meanwhile, the imaginary part increases monotonically with the increasing of the chemical potential; see the top-right panel for the $n = 0$ state and bottom-right panel for the first six quasinormal frequencies. These results were obtained considering $\tilde{q} = 1$ and $\tilde{c} = 0 = \tilde{b}$. As mentioned above, we restrict our results to the region $\tilde{\mu} \leq \sqrt{6}$ where the pseudospectral method provides reliable results. Observing carefully the imaginary part of the frequency in Fig. 13, we can see additional frequencies which are purely imaginary. These frequencies decrease with the increasing of the chemical potential.

Now, one can ask about the behavior of the quasinormal frequencies when one turns on the parameters $c = 1.46\ \mathrm{GeV}^2$ and $b = 0.273\ \mathrm{GeV}^4$. To see how the quasinormal frequencies change in the nonconformal case, we also consider the value of the chemical potential and temperature as being $\mu = \mu_c = 0.708\ \mathrm{GeV}$ and $T = T_c = 0.559\ \mathrm{GeV}$, respectively. Our numerical results for the real part of the frequency are displayed in left panel of Fig. 14 and for the imaginary part of the frequency are displayed in right panel of Fig. 14. In this figure, black dots represent the results for conformal symmetry case, while red squares represent the results for nonconformal case. As can be seen, the real part of the frequency increases, while the imaginary part decreases when we turn on the parameters of the model. Note that lower states are less sensitive to the parameters than higher states. It is also worth mentioning that the precision of the numerical results gets poor when we increase the value of the parameters μ, c, and b.

IX. CONCLUSION

In this paper, we investigated the melting of charmonium in a holographic model describing heavy quark-antiquark systems [46]. The holographic model provides a fit of charmonium masses at zero temperature. For investigating the finite temperature behavior of these states, a black hole was embedded in the gravitational background. In this way, we wrote the perturbation equations in the Schrödinger-like form. This analysis allows us to investigate how the potential well is deformed by the temperature and chemical potential, which is interpreted as the melting/dissociation process. To complement the analysis, we calculated the spectral functions, where peaks are interpreted as the quasiparticle states. We show that the height and width of the peaks are affected by the temperature and chemical potential. These results represent the dissociation of the charmonium states in the finite density plasma. By comparing spectral functions for different temperatures and values of the chemical potential, we observed that the chemical potential speeds up the melting process.

In the second part of this paper, we solved the perturbation equations in the hydrodynamic limit. By imposing Dirichlet condition at the boundary, we calculated the dispersion relations. By comparing the dispersion relation obtained in the longitudinal sector against the dispersion relation obtained in fluid dynamics, we were able to read off the diffusion coefficient. We also showed that the dispersion relation of the longitudinal sector is related to the pole of the $C^R_{tt}(\omega, q)$ retarded function in the dual field theory. Then, we calculated the quark number susceptibility following two approaches. The first approach considers the retarded function $C^R_{tt}(\omega, q)$ in the limit of zero wave number and frequency. The second approach considers the baryon density and its derivative. The quark number susceptibility does not blow up at the critical end point in the first approach, while in the second, it does. The explanation for this apparent discrepancy is that in the first approach one considers the matter action that was introduced as probe fields, while in the second approach, the quark number susceptibility is obtained from the background equations. This result suggests to us that considering probe fields for describing the mesons maybe is not enough to extract full information of the dual field theory.

In the last part of this paper, we solved the perturbation equations numerically using the pseudospectral method. Imposing the ingoing condition at the horizon and Dirichlet at the boundary, we obtained a discrete set of complex frequencies. In the longitudinal sector, we observed very interesting results when we fixed the momentum and varying the chemical potential considering also the parameters $c = 0 = b$. The hydrodynamic mode increases with the chemical potential up to some value of the chemical potential where it merges with a mode whose frequency decreases with the increasing of the chemical potential; see the right panel of Fig. 10. This new mode has a real part arising at exactly the same value of the chemical potential where the hydrodynamic mode merges with this mode. This kind of behavior was previously observed in the literature and is interpreted as a double pole in the retarded Green's function [80]. We found additional frequencies which are purely imaginary, and they decrease with the increasing of the chemical potential. In turn, we also calculated the QN frequencies as a function of the wave number in the conformal and nonconformal limits. The real part of the frequency increases when we compare results obtained in the conformal case, i.e., $c = 0$, $b = 0$, and $\mu = 0$, against results obtained in the nonconformal case, i.e., $c \neq 0$, $b \neq 0$, and $\mu \neq 0$, while the imaginary part decreases when we compared the conformal case against the nonconformal case. These conclusions can be extended for the transverse sector, where the quasinormal frequencies do not bring any new information.

Finally, it would be interesting to investigate how the results obtained in this paper are affected by magnetic field or angular momentum [81,82]. We also are interested in the transport coefficients, which are obtained in the hydrodynamic limit. For example, we believe that the diffusion coefficient will be affected by the rotation parameter in the same form as obtained in Ref. [78]. These problems and further extensions will be addressed in the future.

ACKNOWLEDGMENTS

The authors would like to acknowledge Song He, Alfonso Ballon Bayona, and Alex Miranda for discussions throughout the development of this work. They also thank the referee for valuable suggestions. L. A. H. M. is partially founded by the Universidade Estadual da Região Tocantina do Maranhão (UEMASUL, Brazil). D. F. H. is supported in part by the National Natural Science Foundation of China (NSFC) under Grants No. 11735007, No. 11890711, and No. 35111890710. N. R. F. B. is partially supported by CNPq—Conselho Nacional de Desenvolvimento Cientifico e Tecnologico Grant No. 307641/2015-5, by FAPERJ—Fundação Carlos Chagas Filho de Amparo á Pesquisa do Estado do Rio de Janeiro and by Coordenação de Aperfeiçoamento de Pessoal de Nível Superior—Brasil (CAPES)—Finance Code 001.

APPENDIX: CHARMONIUM SPECTRUM

Introducing the Fourier transform on the gauge field, it transforms as $A^\nu(x^\mu, z) \to A^\nu(k^\mu, z)$. The resulting equation may be written in the Schrödinger-like form using the transformation $A_\nu = \xi_\nu e^{-B}\psi$, where ξ_ν is a polarization vector and $2B = \ln(f/\zeta)$, and the resulting equation is

$$-\partial_z^2\psi + V\psi = m^2\psi, \tag{A1}$$

where we have replaced $\Box \to m^2$, the mass of the particles, and V is the potential given by

$$V = (\partial_z B)^2 + \partial_z^2 B. \tag{A2}$$

As the background was already fixed, we may solve the eigenvalue problem using a shooting method, for example. It is worth pointing out that the ratio f/ζ does not depend on the parameter b, and for that reason, the spectrum is insensitive to this parameter. Thus, in this case, the problem has an analytic solution given by

$$m_n^2 = 4c(n+1), \quad n = 0, 1, 2, \ldots. \tag{A3}$$

In the sequence, we fix the free parameter by fitting our formula with the first two resonances of the experimental data 3686.109 ± 0.012 MeV and 4039 ± 1 MeV; thus, we get $c = 1.46\ \mathrm{GeV}^2$. We decided to fix the parameter in this wave to avoid the lightest states. The numerical results of the spectrum compared against the results of Ref. [46] and experimental data are displayed in Table. V.

Here, we presented the asymptotic solutions of the differential equations. Let us start with the model at zero temperature. Plugging the warp factor and kinetic function (8) in (23), the potential of the Schrödinger-like equation becomes

$$V = \frac{3}{4z^2} + c^2 z^2. \tag{A4}$$

As can be seen, the spectrum does not depend on the parameter b. Plugging the potential in the Schrödinger-like

TABLE V. The mass of the heavy vector mesons (in MeV) obtained in the holographic model, compared against the holographic model [46] and experimental results from the Particle Data Group [58].

n	Model $c =$ 1.46 GeV^2	Model $c =$ 1.16 GeV^2 [46]	Quarkonium experimental [58] (MeV)
0	2420	2154	3096.916 ± 0.011
1	3422	3046	3686.109 ± 0.012
2	4191	3731	4039 ± 1
3	4839		4421 ± 4

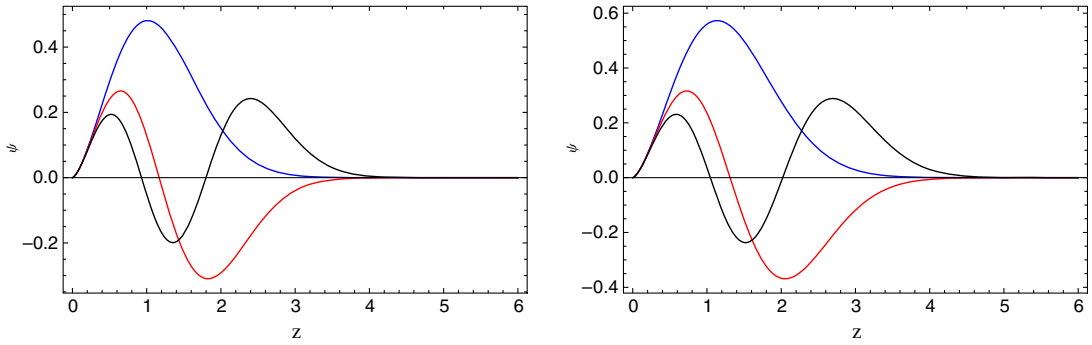

FIG. 15. Left: the wave functions for $c = 1.46$ GeV^2. Right: the wave functions for $c = 1.16$ GeV^2.

equation (22) and considering the ansatz, $\psi = z^{\alpha}$, close to the boundary, we get the solution

$$\psi = c_1 z^{-1/2} + c_2 z^{3/2}. \tag{A5}$$

As we are looking for normalizable solutions of the eigenvalue problem, we set $c_1 = 0$.

In turn, in the IR regime, the asymptotic solution may be obtained considering the leading term of the potential; thus, solving the Schrödinger-like equation, we get

$$\psi = c_3 e^{-cz^2/2}. \tag{A6}$$

As the background does not have any singular behavior in the intermediate region, we conclude that the solutions of the Schrödinger-like equation are regular and normalizable.

On the other hand, the problem changes at finite temperature. At the horizon, the potential is zero due to $g(z_h) = 0$. Then, the Schrödinger-like equations have the asymptotic solution

$$\psi_k = C_k e^{-i\omega r_*} + D_k e^{+i\omega r_*}, \qquad (k = x^1, x^2, x^3). \tag{A7}$$

Considering the parameter $c = 1.46$ GeV^2, we calculate the wave functions. Our numerical results are displayed in the left panel of Fig. 15, while the right panel shows the wave functions for $c = 1.16$ GeV^2 calculated in Ref. [46].

[1] T. Matsui and H. Satz, Phys. Lett. B **178**, 416 (1986).
[2] R. Ma, Nucl. Phys. **A982**, 120 (2019).
[3] F. Karsch, Eur. Phys. J. C **43**, 35 (2005).
[4] E. V. Shuryak, *The QCD Vacuum, Hadrons and the Superdense Matter*, World Scientific Lecture Notes in Physics Volume 71 (World Scientific, Singapore, 1988), Vol. 8.
[5] J. M. Maldacena, Adv. Theor. Math. Phys. **2**, 231 (1998).
[6] E. Witten, Adv. Theor. Math. Phys. **2**, 253 (1998).
[7] S. S. Gubser, I. R. Klebanov, and A. M. Polyakov, Phys. Lett. B **428**, 105 (1998).
[8] J. Polchinski and M. J. Strassler, Phys. Rev. Lett. **88**, 031601 (2002).
[9] H. Boschi-Filho and N. R. F. Braga, Eur. Phys. J. C **32**, 529 (2004).
[10] H. Boschi-Filho and N. R. F. Braga, J. High Energy Phys. 05 (2003) 009.
[11] A. Cherman, T. D. Cohen, and E. S. Werbos, Phys. Rev. C **79**, 045203 (2009).
[12] Z. Abidin and C. E. Carlson, Phys. Rev. D **80**, 115010 (2009).
[13] T. Gherghetta, J. I. Kapusta, and T. M. Kelley, Phys. Rev. D **79**, 076003 (2009).
[14] K. Chelabi, Z. Fang, M. Huang, D. Li, and Y.-L. Wu, J. High Energy Phys. 04 (2016) 036.
[15] A. Ballon-Bayona and L. A. H. Mamani, Phys. Rev. D **102**, 026013 (2020).
[16] K. Ghoroku, N. Maru, M. Tachibana, and M. Yahiro, Phys. Lett. B **633**, 602 (2006).
[17] P. Colangelo, F. De Fazio, F. Giannuzzi, F. Jugeau, and S. Nicotri, Phys. Rev. D **78**, 055009 (2008).
[18] H. R. Grigoryan and A. V. Radyushkin, Phys. Rev. D **76**, 115007 (2007).
[19] A. Vega and I. Schmidt, Phys. Rev. D **78**, 017703 (2008).
[20] H. J. Kwee and R. F. Lebed, J. High Energy Phys. 01 (2008) 027.
[21] P. Colangelo, F. Giannuzzi, and S. Nicotri, Phys. Rev. D **80**, 094019 (2009).
[22] A. S. Miranda, C. A. Ballon Bayona, H. Boschi-Filho, and N. R. F. Braga, J. High Energy Phys. 11 (2009) 119.
[23] L. A. H. Mamani, A. S. Miranda, H. Boschi-Filho, and N. R. F. Braga, J. High Energy Phys. 03 (2014) 058.
[24] D. Dudal and T. G. Mertens, Phys. Rev. D **91**, 086002 (2015).

[25] L. A. H. Mamani, A. S. Miranda, and V. T. Zanchin, Eur. Phys. J. C **79**, 435 (2019).
[26] S. P. Bartz and J. I. Kapusta, J. Phys. Conf. Ser. **446**, 012019 (2013).
[27] L.-X. Cui, S. Takeuchi, and Y.-L. Wu, J. High Energy Phys. 04 (2012) 144.
[28] M. Fujita, K. Fukushima, T. Misumi, and M. Murata, Phys. Rev. D **80**, 035001 (2009).
[29] M. Fujita, T. Kikuchi, K. Fukushima, T. Misumi, and M. Murata, Phys. Rev. D **81**, 065024 (2010).
[30] N. R. F. Braga, M. A. Martin Contreras, and S. Diles, Phys. Lett. B **763**, 203 (2016).
[31] N. R. F. Braga, M. A. Martin Contreras, and S. Diles, Europhys. Lett. **115**, 31002 (2016).
[32] N. R. F. Braga, M. A. Martin Contreras, and S. Diles, Eur. Phys. J. C **76**, 598 (2016).
[33] N. R. F. Braga, L. F. Ferreira, and A. Vega, Phys. Lett. B **774**, 476 (2017).
[34] N. R. F. Braga and L. F. Ferreira, Phys. Lett. B **773**, 313 (2017).
[35] N. R. F. Braga and R. Da Mata, Phys. Lett. B **804**, 135381 (2020).
[36] N. R. F. Braga and L. F. Ferreira, Phys. Lett. B **795**, 462 (2019).
[37] C. Csaki and M. Reece, J. High Energy Phys. 05 (2007) 062.
[38] U. Gursoy, E. Kiritsis, and F. Nitti, J. High Energy Phys. 02 (2008) 019.
[39] U. Gursoy, E. Kiritsis, L. Mazzanti, and F. Nitti, J. High Energy Phys. 05 (2009) 033.
[40] S. S. Gubser, A. Nellore, S. S. Pufu, and F. D. Rocha, Phys. Rev. Lett. **101**, 131601 (2008).
[41] D. Li and M. Huang, J. High Energy Phys. 11 (2013) 088.
[42] A. Ballon-Bayona, H. Boschi-Filho, L. A. H. Mamani, A. S. Miranda, and V. T. Zanchin, Phys. Rev. D **97**, 046001 (2018).
[43] A. Ballon-Bayona, L. A. H. Mamani, A. S. Miranda, and V. T. Zanchin, Phys. Rev. D **104**, 046013 (2021).
[44] W. de Paula, T. Frederico, H. Forkel, and M. Beyer, Phys. Rev. D **79**, 075019 (2009).
[45] D. Li, S. He, and M. Huang, J. High Energy Phys. 06 (2015) 046.
[46] S. He, S.-Y. Wu, Y. Yang, and P.-H. Yuan, J. High Energy Phys. 04 (2013) 093.
[47] Y. Yang and P.-H. Yuan, J. High Energy Phys. 11 (2014) 149.
[48] D. Dudal and T. G. Mertens, Phys. Rev. D **97**, 054035 (2018).
[49] D. Dudal and S. Mahapatra, Phys. Rev. D **96**, 126010 (2017).
[50] L. A. H. Mamani, C. V. Flores, and V. T. Zanchin, Phys. Rev. D **102**, 066006 (2020).
[51] A. Ballon-Bayona, H. Boschi-Filho, E. F. Capossoli, and D. M. Rodrigues, Phys. Rev. D **102**, 126003 (2020).
[52] X. Chen, D. Li, and M. Huang, Chin. Phys. C **43**, 023105 (2019).
[53] S. He, Y. Yang, and P.-H. Yuan, arXiv:2004.01965.
[54] Note that we are using the negative sign of the kinetic function exponent. This is motivated by the original holographic soft wall model [55]; for a recent discussion on the sign of the soft wall model, see Ref. [56].
[55] A. Karch, E. Katz, D. T. Son, and M. A. Stephanov, Phys. Rev. D **74**, 015005 (2006).
[56] A. Ballon-Bayona, L. A. H. Mamani, and D. M. Rodrigues, Phys. Rev. D **104**, 126029 (2021).
[57] M. Ammon and J. Erdmenger, *Gauge/Gravity Duality: Foundations and Applications* (Cambridge University Press, Cambridge, England, 2015).
[58] M. Tanabashi *et al.* (Particle Data Group), Phys. Rev. D **98**, 030001 (2018).
[59] Note that the value of $c = 1.46\ \mathrm{GeV}^2$ is slightly different from the value used in Ref. [46]; see Appendix for discussion about the value we are using.
[60] X. Cao, S. Qiu, H. Liu, and D. Li, J. High Energy Phys. 08 (2021) 005.
[61] D. T. Son and A. O. Starinets, J. High Energy Phys. 09 (2002) 042.
[62] Y.-Q. Zhao and D. Hou, arXiv:2108.08479.
[63] P. K. Kovtun and A. O. Starinets, Phys. Rev. D **72**, 086009 (2005).
[64] Y. Kim, Y. Matsuo, W. Sim, S. Takeuchi, and T. Tsukioka, J. High Energy Phys. 05 (2010) 038.
[65] Y. Kim, S.-J. Sin, K. H. Jo, and H. K. Lee, arXiv:hep-ph/0609008.
[66] D.-k. He, X.-x. Ruan, Y. Jiang, W.-M. Sun, and H.-S. Zong, Phys. Lett. B **680**, 432 (2009).
[67] K. Jo, Y. Kim, H. K. Lee, and S.-J. Sin, J. High Energy Phys. 11 (2008) 040.
[68] K.-i. Kim, Y. Kim, S. Takeuchi, and T. Tsukioka, Prog. Theor. Phys. **126**, 735 (2011).
[69] M. He, J.-F. Li, W.-M. Sun, and H.-S. Zong, Phys. Rev. D **79**, 036001 (2009).
[70] A. Bzdak, S. Esumi, V. Koch, J. Liao, M. Stephanov, and N. Xu, Phys. Rep. **853**, 1 (2020).
[71] B. Friman, F. Karsch, K. Redlich, and V. Skokov, Eur. Phys. J. C **71**, 1694 (2011).
[72] S. Borsanyi, Z. Fodor, J. N. Guenther, S. K. Katz, K. K. Szabo, A. Pasztor, I. Portillo, and C. Ratti, J. High Energy Phys. 10 (2018) 205.
[73] J. P. Boyd, *Chebyshev and Fourier Spectral Methods*, 2nd ed., Dover Books on Mathematics (Dover Publications, Mineola, NY, 2001).
[74] A. Jansen, Eur. Phys. J. Plus **132**, 546 (2017).
[75] R. Rougemont, R. Critelli, and J. Noronha, Phys. Rev. D **98**, 034028 (2018).
[76] S. I. Finazzo, R. Rougemont, M. Zaniboni, R. Critelli, and J. Noronha, J. High Energy Phys. 01 (2017) 137.
[77] L. A. H. Mamani, A. D. Masa, L. T. Sanches, and V. T. Zanchin, Revisiting the quasinormal modes of the Schwarzschild black hole: Numerical analysis, (2022), arXiv:2206.03512.
[78] L. A. H. Mamani, J. Morgan, A. S. Miranda, and V. T. Zanchin, Phys. Rev. D **98**, 026006 (2018).
[79] G. B. Cook and M. Zalutskiy, Classical Quantum Gravity **33**, 245008 (2016).
[80] A. S. Miranda, J. Morgan, and V. T. Zanchin, J. High Energy Phys. 11 (2008) 030.
[81] X. Chen, L. Zhang, D. Li, D. Hou, and M. Huang, J. High Energy Phys. 07 (2021) 132.
[82] N. R. F. Braga, L. F. Faulhaber, and O. C. Junqueira, Phys. Rev. D **105**, 106003 (2022).